Supporting Information for the manuscript:

A family of dioxyarylene linked di-o-quinones. Structural dependence on the topology of linker: comparative study.

Anna V. Cherkasova, Konstantin A. Martyanov, Elena A. Rychagova, Konstantin A. Kozhanov, Anton V. Cherkasov, Viacheslav A. Kuropatov*

Table of Contents

X-ray diffractometry data

According to SC XRD data, **2-4** are two o-dioxolene moieties linked with 2,4-di-tertbutyl-*m*-dioxyphenylene (**2**), 2,7-dioxynaphthalene (**3**), and p-dioxyphenylene (**4**) *via* phenoxyl groups. All samples are crystallized with crystallographically unique molecules in the asymmetric part of the unit cells with no solvent molecules. The o-quinone nature of dioxolene fragments is clearly confirmed by C=O and C-C bond lengths distribution (Table X1). The O-C-C-O$_{quinone}$ torsion angles in **2** (1.3(3), 6.3(3)°) are much closer comparable to **1** (11.4(3), 12.6(2)°), **3** (18.1(5), 28.2(5)°) and **4** (12.9(5), 27.5(4)°). Thus, while in **1**, **3**, and **4** the steric interaction of bulk ^{t}Bu-groups with carbonyl oxygen atoms leads to distortion of the OCCO-fragment, this doesn't occur in **2**. It's important to note that in **3** the naphthalene linker is completely disordered by two sites, but this doesn't affect the mutual position of the quinone moieties.

As the previous work, to describe the topology of **2-4** molecular structures two geometric parameters were chosen – the torsion angle between the C$_{dioxolene}$-O$_{phenoxyl}$ bonds (τ) and the dihedral angle between the mean planes of the dioxolene fragments (*d*). The τ and *d* in **2** are 62.2(2)° and 22.76(5)°, respectively, and comparable with those in **1** (τ 42.4(2)°, *d* 27.67(5)°). It's easy to see that the arrangement of the *o*-dioxolene mean planes in **1** and **2** is close to parallel. Moreover, even though τ in **2** is slightly wider than in **1**, the potential coordination vectors of *o*-quinone ligands in **2** can still be defined as codirectional. The torsional angle in **3** is even closer, but the dihedral angle between the planes is much larger than in **2**. Apparently, the larger steric size of the 2,7-dioxynaphthalene linker in **3** compared to the *m*-dioxyphenylene in **1** and **2** is the key factor determining the mutual arrangement of the quinone fragments in this case. Being further away from each other, they can rotate along the C$_{dioxolene}$-O$_{phenoxyl}$ bond without affecting each other with bulk tert-butyl substituents.

The linker design in **4** distinguishes this compound from all previously described ones. Thus, due to the location of phenoxyl groups in the para-positions, the coordination vectors of the quinone fragments are directed in different ways from each other. At the same time, the arrangement of these fragments is still close to parallel, as in **1** and **2**. We believe that di-o-quinone **4** is of interest as a building block suitable for the construction of MOFs with large internal cavity volumes.
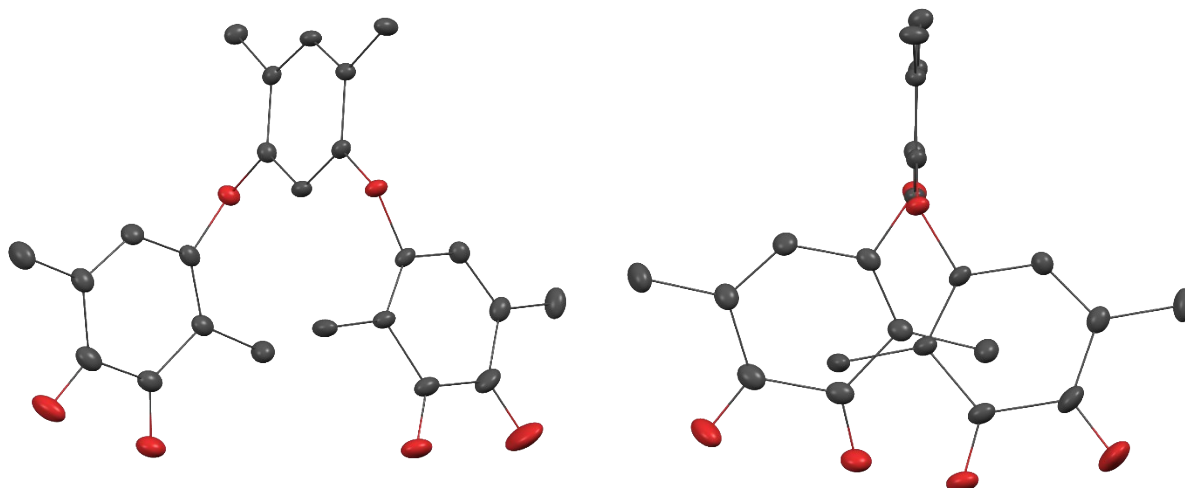

Figure SI1. Molecular structure of **2**. Thermal ellipsoids are given at 30% probability level. Hydrogen atoms and methyl groups of *tert*-butyl substituents are omitted for clarity. Color code: C, black; O, red.
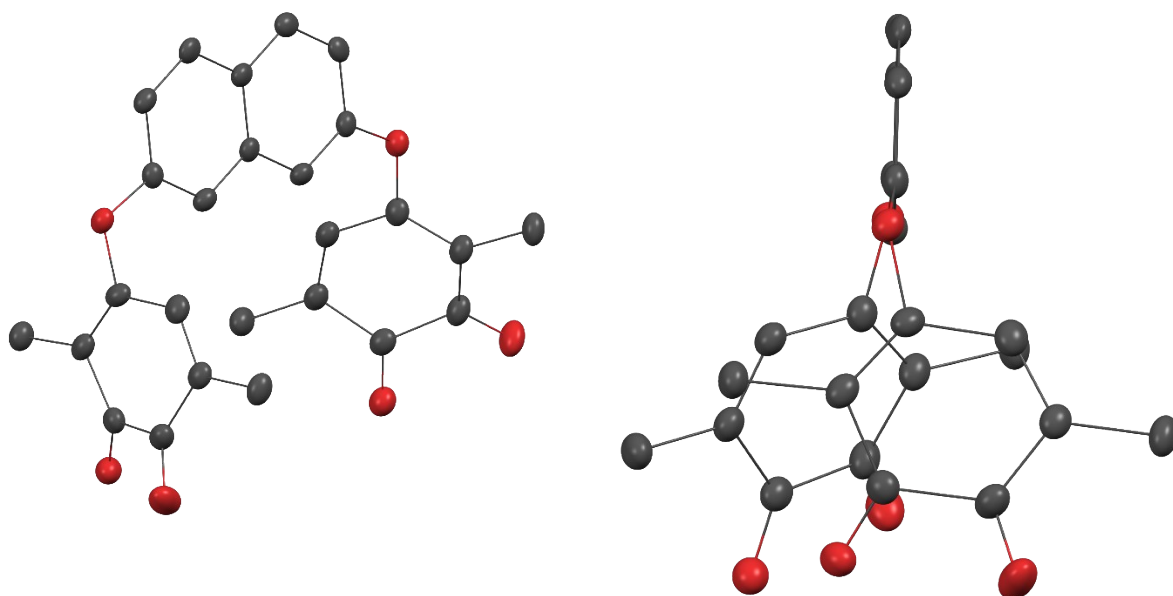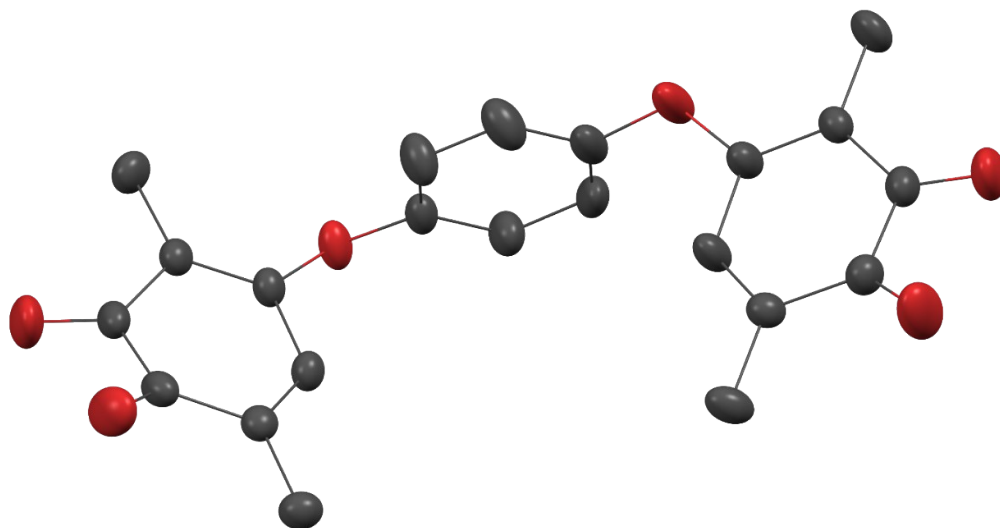
Figure SI2. Molecular structure of **3**. Thermal ellipsoids are given at 30% probability level. Hydrogen atoms and methyl groups of tert-butyl substituents are omitted for clarity. Color code: C, black; O, red.

Figure SI3. Molecular structure of **4**. Thermal ellipsoids are given at 30% probability level. Hydrogen atoms and methyl groups of tert-butyl substituents are omitted for clarity. Color code: C, black; O, red.

Table SI1. The selected bond lengths (Å) and torsion angles (deg.) for **2-4**.

	2	3	4
C=O$_{quinone}$	1.216(2)	1.214(4)	1.205(3)
	1.218(2)	1.216(4)	1.208(3)
	1.222(2)	1.218(4)	1.209(3)
	1.222(2)	1.221(4)	1.217(3)
C-C$_{quinone}$	1.556(3)	1.561(5)	1.540(4)
	1.559(3)	1.566(5)	1.545(4)
C$_{dioxolene}$-O$_{phenoxyl}$	1.381(2)	1.375(3)	1.381(3)
	1.390(2)	1.382(5)	1.374(3)
		1.386(3)	
O-C-C-O$_{quinone}$	1.3(3)	18.1(5)	12.9(5)
	6.3(3)	28.2(5)	27.5(4)
τ	65.2(2)	2.1(8)	69.2(3)
		27.1(2)	
d	22.76(5)	53.15(8)	28.0(2)

Table SI2. The crystal data and structure refinement details for **2-4**.

	2	3	4
Formula	C$_{42}$H$_{58}$O$_6$	C$_{38}$H$_{44}$O$_6$	C$_{34}$H$_{42}$O$_6$
M	658.88	596.73	546.67
T, K	100.0(2)	100.0(2)	298.0(2)
λ, Å	0.71073	0.71073	0.71073
Crystal system	Monoclinic	Monoclinic	Monoclinic
Space group	$P2_1/n$	$P2_1/c$	$P2_12_12_1$
a, Å	11.3903(4)	11.8467(10)	10.2098(3)
b, Å	15.3731(5)	25.0666(13)	10.4124(3)
c, Å	24.4921(9)	12.2051(9)	29.8234(9)
α, deg	90	90	90
β, deg	90.899(3)	113.534(9)	90
γ, deg	90	90	90

V, Å^3	4288.1(3)	3322.9(5)	3170.48(16)
Z	4	4	4
d_{calc}, g/cm$_3$	1.021	1.193	1.145
μ, mm^{-1}	0.067	0.079	0.077
F_{000}	1432	1280	1176
Crystal dimensions, mm	0.70×0.45×0.20	0.57×0.35×0.20	0.69×0.57×0.40
ϑ range for data collection, deg	2.37–28.70	3.04–25.03	3.11–30.03
Completeness, %	99.6	99.8	99.7
HKL indices	$-15 \le h \le 15$	$-14 \le h \le 14$	$-14 \le h \le 14$
	$-20 \le k \le 20$	$-29 \le k \le 29$	$-14 \le k \le 14$
	$-33 \le l \le 33$	$-14 \le l \le 14$	$-42 \le l \le 41$
Reflns. Collected	98130	45117	62009
Reflns. unique ($I > 2\sigma(I)$)	9341	4002	8079
R_{int}	0.1073	0.0683	0.0180
Data / restraints / parameters	19340 / 402 / 452	5851 / 9 / 401	9276 / 480 / 473
$S(F^2)$	0.996	1.071	1.058
R_1 / wR_2 ($I > 2\sigma(I)$)	0.0547 / 0.1089	0.0759 / 0.1687	0.0589 / 0.1726
R_1 / wR_2 (all data)	0.1089 / 0.1206	0.1126 / 0.1884	0.0660 / 0.1801
Largest diff. peak and hole, e/Å^3	0.23 / -0.27	0.38 / -0.37	0.58 / -0.29

Cyclic voltammetry
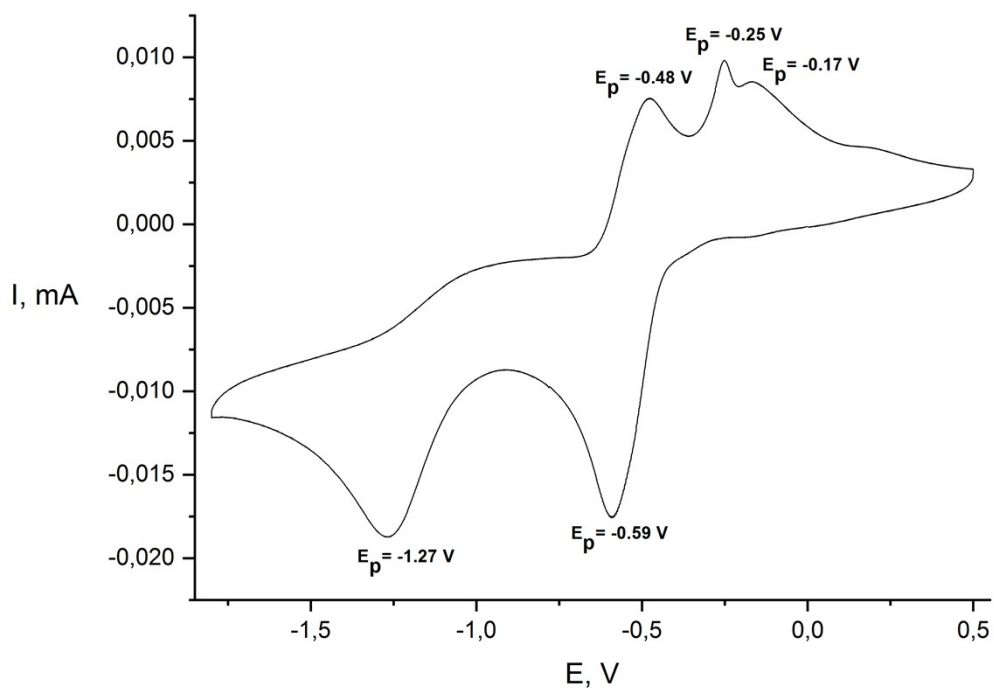
Figure SI4. Cyclic voltammogram of di-o-quinone **3** (1.0 × 10^{-3} M in CH$_2$Cl$_2$, 200 mV s^{-1}, 0.2 M Bu$_4$NClO$_4$)
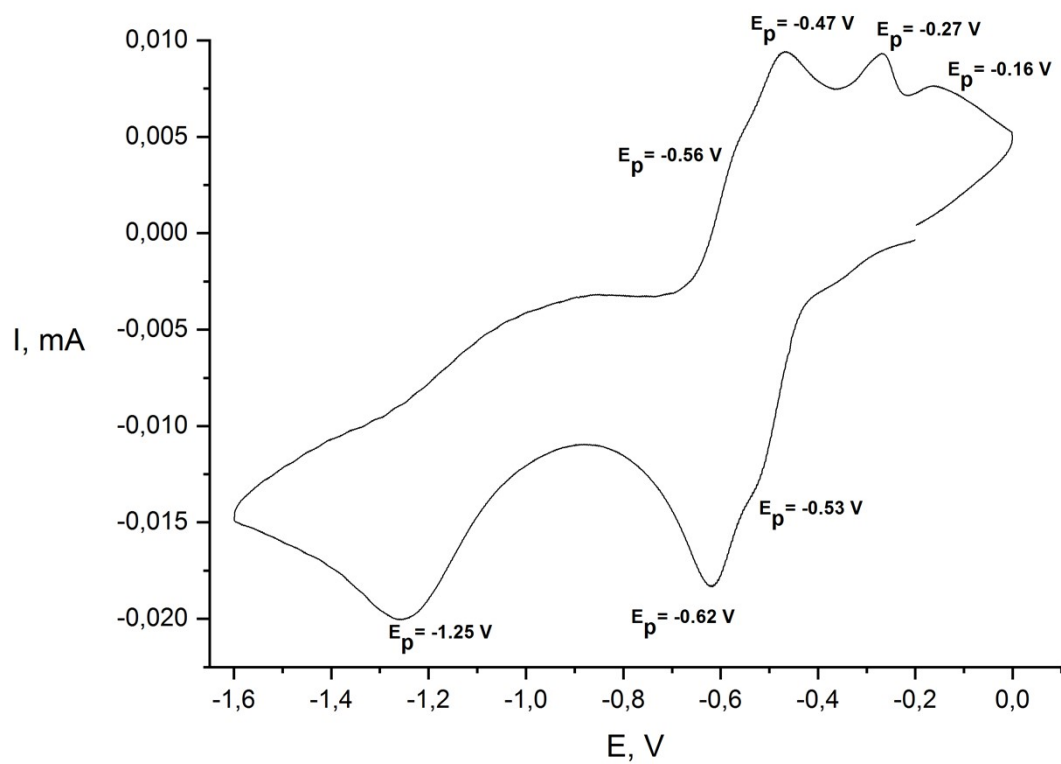
Figure SI5. Cyclic voltammogram of di-o-quinone **4** (1.0 × 10^{-3} M in CH$_2$Cl$_2$, 200 mV s^{-1}, 0.2 M Bu$_4$NClO$_4$)

EPR spectra
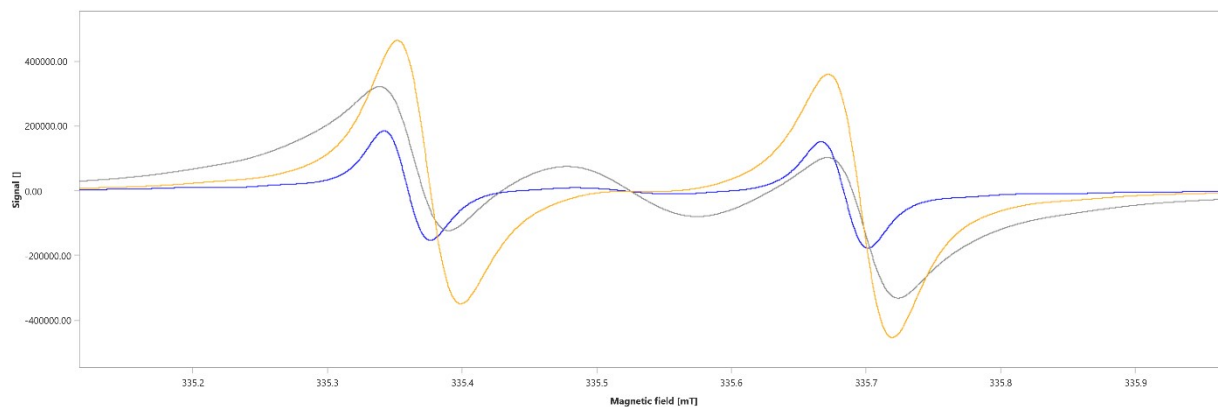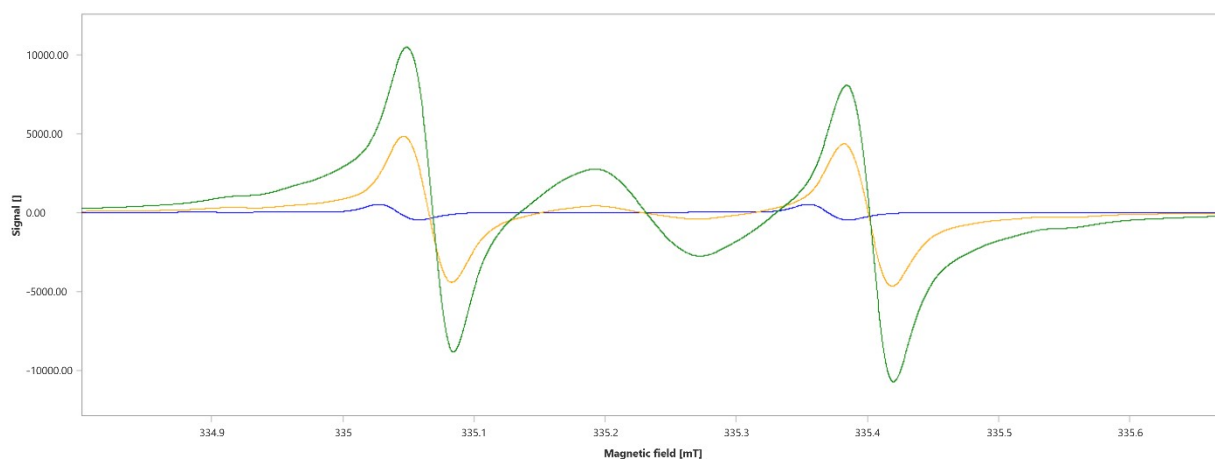

Figure SI6. Evolution of EPR spectrum during the reduction of **1** with K in THF, 293K: brown line- **Q-O-*Lnk*-O-SQ$^{.-}$K$^+$**; gray line - **K$^+$SQ$^{.-}$-O-*Lnk*-O-SQ$^{.-}$K$^+$**; blue line - **K$^+$SQ$^{.-}$-O-*Lnk*-O-Cat^{2-} K$_2$$^{2+}$**

Figure SI7. Evolution of EPR spectrum during the reduction of **1** with Tl in THF, 293K: green line- **Q-O-*Lnk*-O-SQ$^{.-}$Tl$^+$**; brown line - **Tl$^+$SQ$^{.-}$-O-*Lnk*-O-SQ$^{.-}$Tl$^+$**; blue line - **Tl$^+$SQ$^{.-}$-O-*Lnk*-O-Cat^{2-}Tl$_2$$^{2+}$**
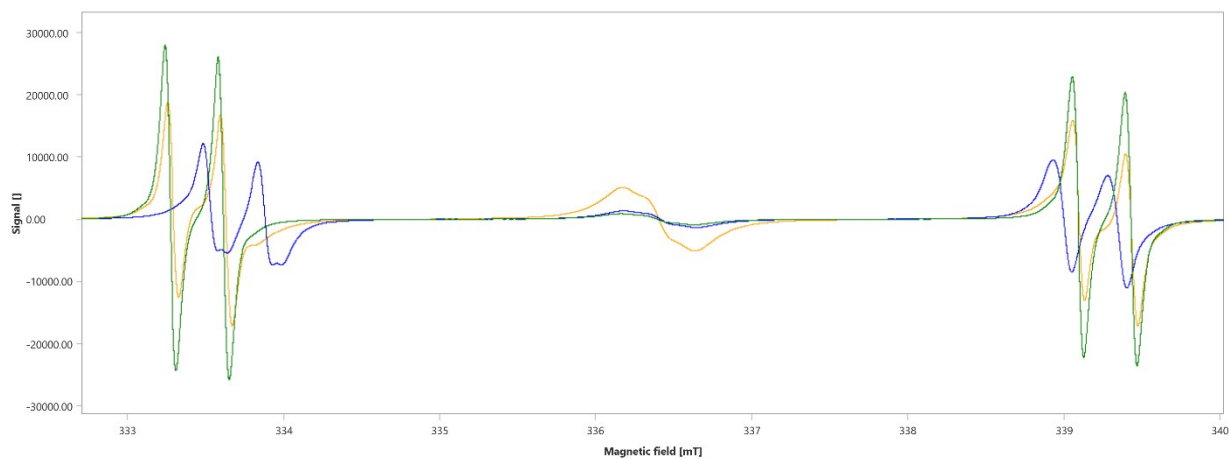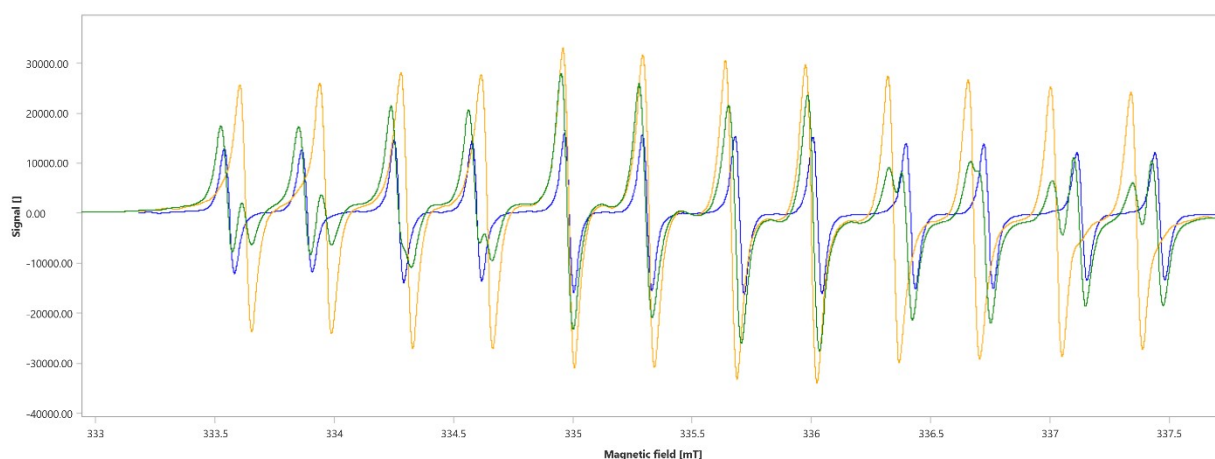
Figure SI8. Evolution of EPR spectrum during the reduction of **1** with Mn$_2$(CO)$_{10}$ in toluene, 293K: green line- **Q-O-*Lnk*-O-SQ$^{.-}$Mn(CO)$_4$$^+$**; blue line – **(CO)$_4Mn^+SQ^{.-}$-O-*Lnk*-O-SQ$^{.-}$Mn(CO)$_4$$^+$**; brown line - **(CO)$_4Mn^+SQ^{.-}$-O-*Lnk*-O-Cat^{2-}[Mn(CO)$_4$]$_2$$^{2+}$**
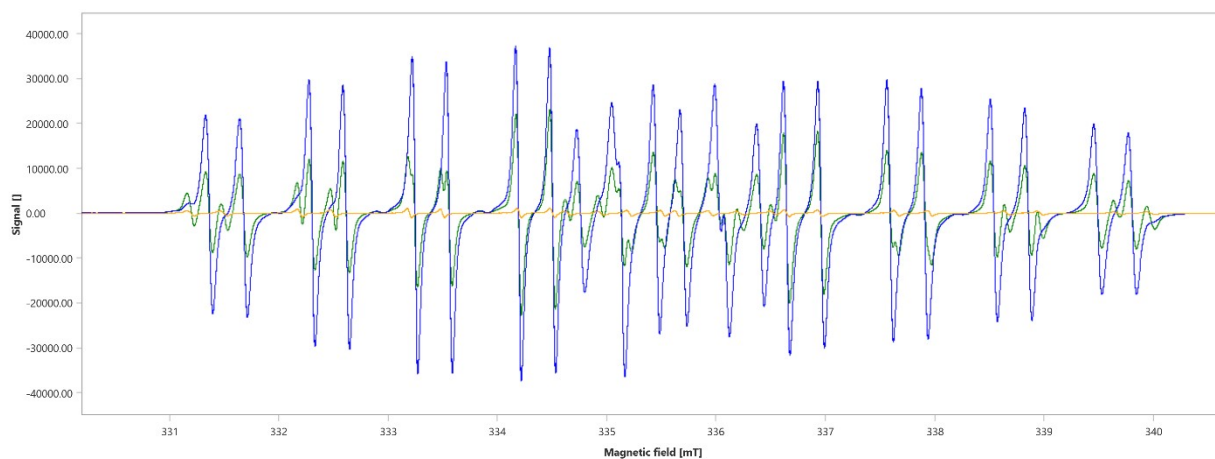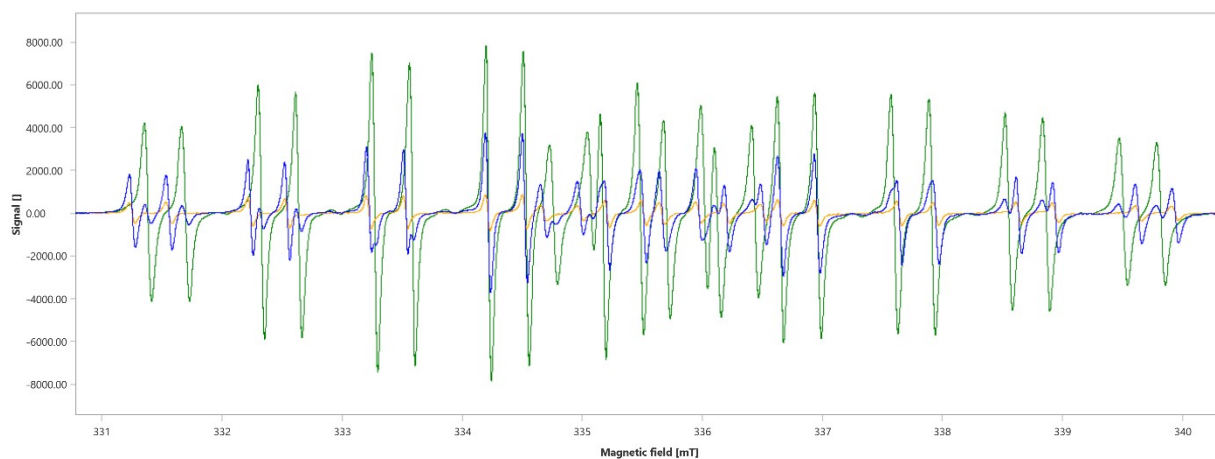
Figure SI9. Evolution of EPR spectrum during the reduction of **1** with $Mn_2(CO)_{10}$ in the presence of PPh_3 in toluene, 293K: brown line- **Q-O-*Lnk*-O-SQ$^{\cdot-}$ Mn(PPh$_3$)(CO)$_3^+$**; green line – **(CO)$_3$(PPh$_3$)Mn$^+$SQ$^{\cdot-}$-O-*Lnk*-O-SQ$^{\cdot-}$ Mn(PPh$_3$)(CO)$_3^+$**; blue line - **(CO)$_3$(PPh$_3$)Mn$^+$SQ$^{\cdot-}$-O-*Lnk*-O-Cat^{2-}[Mn(PPh$_3$)(CO)$_3$]$_2^{2+}$**
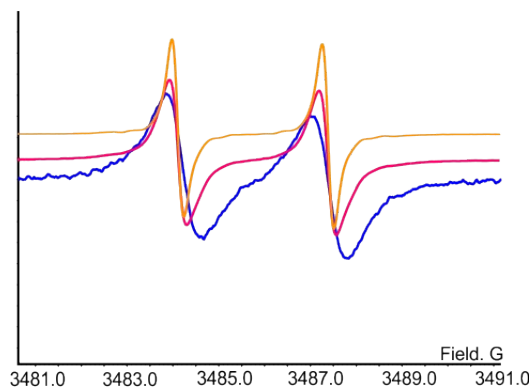
Figure SI10. Evolution of EPR spectrum during the electrochemical reduction of **1** in CH$_2$Cl$_2$, 0.1 M Bu$_4$NClO$_4$, 293K: blue line- **Q-O-*Lnk*-O-SQ$^{\cdot-}$**; red line –**SQ$^{\cdot-}$-O-*Lnk*-O-SQ$^{\cdot-}$**; brown line - **SQ$^{\cdot-}$-O-*Lnk*-O-Cat^2**
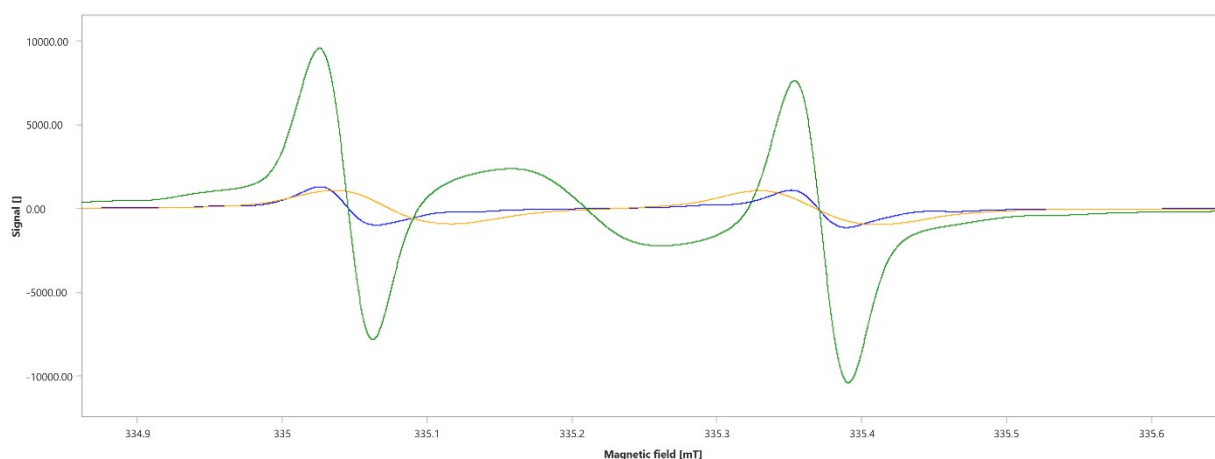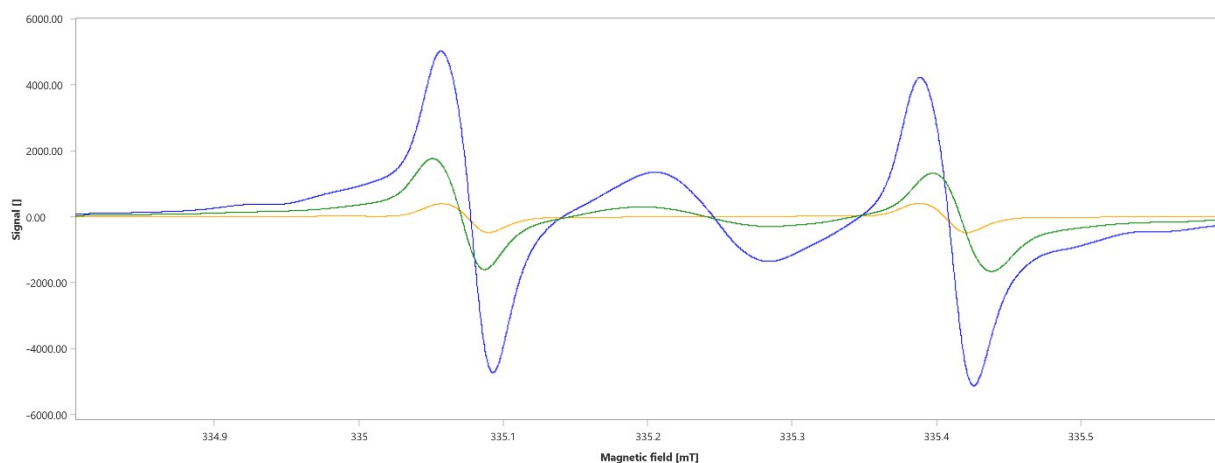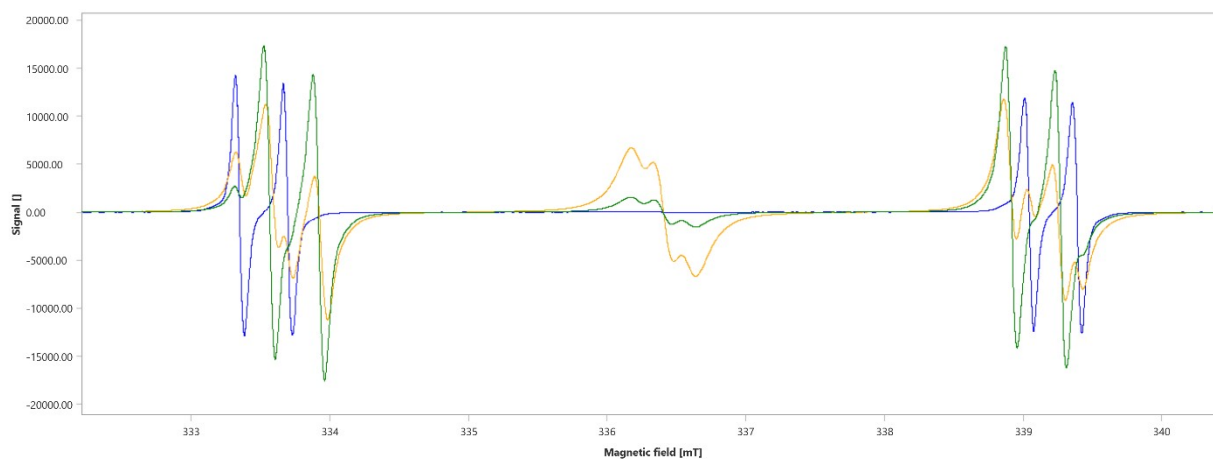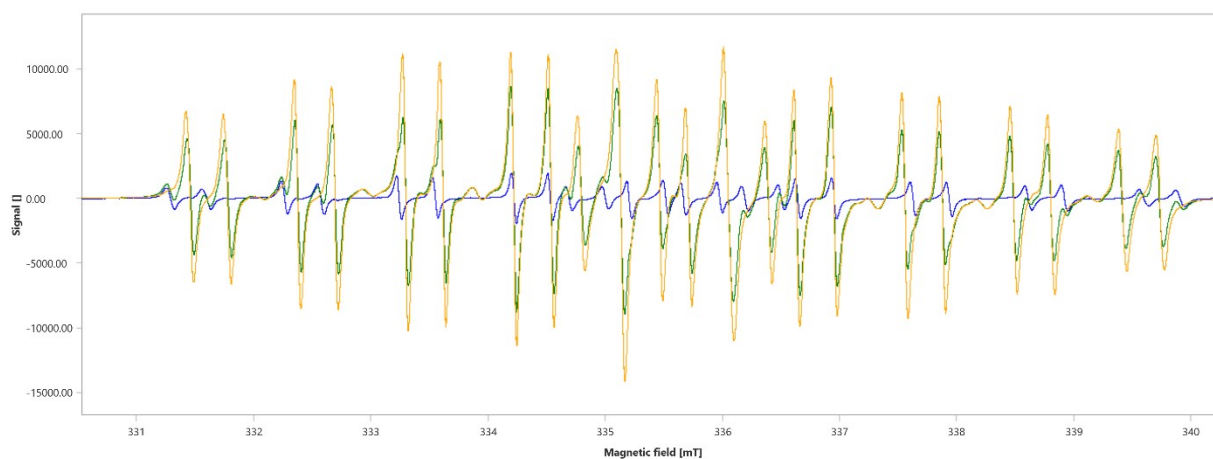

Figure SI11. Evolution of EPR spectrum during the reduction of **2** with K in THF, 293K: blue line- **Q-O-*Lnk*-O-SQ$^{\cdot-}$K$^+$**; green line - **K$^+$SQ$^{\cdot-}$-O-*Lnk*-O-SQ$^{\cdot-}$K$^+$**; brown line - **K$^+$SQ$^{\cdot-}$-O-*Lnk*-O-Cat^{2-} K$_2^{2+}$**
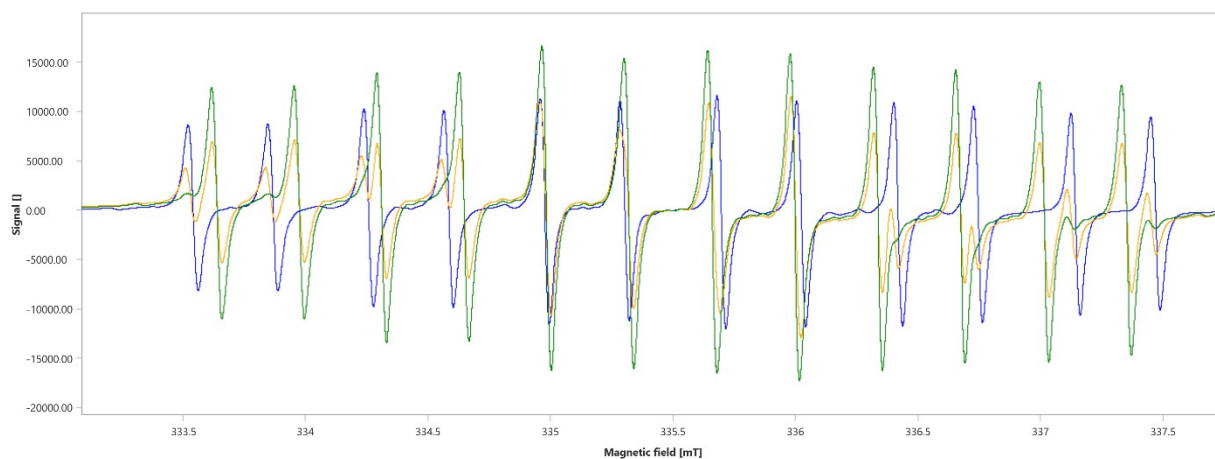
Figure SI12. Evolution of EPR spectrum during the reduction of **2** with $Mn_2(CO)_{10}$ in toluene, 293K: blue line- **Q-O-*Lnk*-O-SQ·⁻Mn(CO)₄⁺**; brown line – **(CO)₄Mn⁺SQ·⁻-O-*Lnk*-O-SQ·⁻Mn(CO)₄⁺**; blue line - **(CO)₄Mn⁺SQ·⁻-O-*Lnk*-O-Cat²⁻[Mn(CO)₄]₂²⁺**
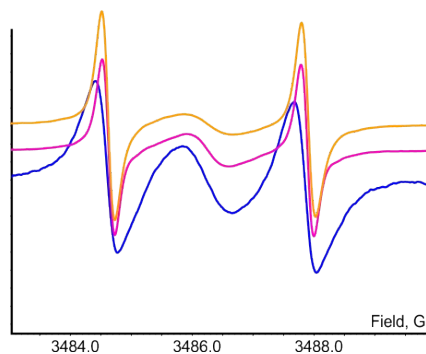
Figure SI13. Evolution of EPR spectrum during the electrochemical reduction of **2** in CH_2Cl_2, 0.1 M Bu₄NClO₄, 293K: blue line- **Q-O-*Lnk*-O-SQ·⁻**; red line –**SQ·⁻-O-*Lnk*-O-SQ·⁻**; brown line - **SQ·⁻-O-*Lnk*-O-Cat²**

Figure SI14. Evolution of EPR spectrum during the reduction of **3** with K in THF, 293K: brown line- **Q-O-*Lnk*-O-SQ·⁻K⁺**; green line - **K⁺SQ·⁻-O-*Lnk*-O-SQ·⁻K⁺**; blue line - **K⁺SQ·⁻-O-*Lnk*-O-Cat²⁻ K₂²⁺**

Figure SI15. Evolution of EPR spectrum during the reduction of **3** with $Mn_2(CO)_{10}$ in the presence of PPh_3 in toluene, 293K: brown line- **Q-O-*Lnk*-O-SQ·⁻ Mn(PPh₃)(CO)₃⁺**; blue line – **(CO)₃(PPh₃)Mn⁺SQ·⁻-O-*Lnk*-O-SQ·⁻ Mn(PPh₃)(CO)₃⁺**; green line - **(CO)₃(PPh₃)Mn ⁺SQ·⁻-O-*Lnk*-O-Cat²⁻[Mn(PPh₃)(CO)₃]₂²⁺**
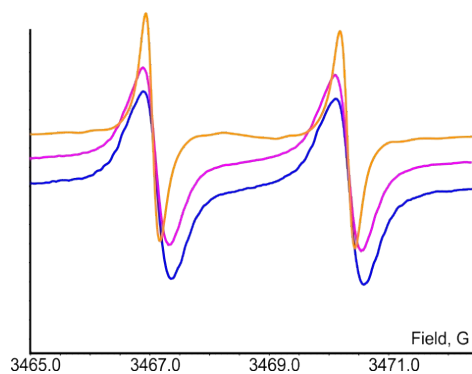
Figure SI16. Evolution of EPR spectrum during the electrochemical reduction of **3** in CH_2Cl_2, 0.1 M Bu_4NClO_4, 293K: blue line- **Q-O-*Lnk*-O-SQ·⁻**; red line –**SQ·⁻-O-*Lnk*-O-SQ·⁻**; brown line - **SQ·⁻-O-*Lnk*-O-Cat²**

Figure SI17. Evolution of EPR spectrum during the reduction of **4** with K in THF, 293K: brown line- **Q-O-*Lnk*-O-SQ·⁻K⁺**; blue line - **K⁺SQ·⁻-O-*Lnk*-O-SQ·⁻K⁺**; green line - **K⁺SQ·⁻-O-*Lnk*-O-Cat²⁻ K₂²⁺**

Figure SI18. Evolution of EPR spectrum during the reduction of **4** with Tl in THF, 293K: blue line- **Q-O-*Lnk*-O-SQ⁻Tl⁺**; brown line - **Tl⁺SQ·⁻-O-*Lnk*-O-SQ·⁻Tl⁺**; green line - **Tl⁺SQ·⁻-O-*Lnk*-O-Cat²⁻Tl₂²⁺**

Figure SI19. Evolution of EPR spectrum during the reduction of **4** with $Mn_2(CO)_{10}$ in the presence of PPh_3 in toluene, 293K: blue line- **Q-O-*Lnk*-O-SQ·⁻ Mn(PPh₃)(CO)₃⁺**; brown line – **(CO)₃(PPh₃)Mn⁺SQ·⁻-O-*Lnk*-O-SQ·⁻ Mn(PPh₃)(CO)₃⁺**; green line - **(CO)₃(PPh₃)Mn ⁺SQ·⁻-O-*Lnk*-O-Cat²⁻[Mn(PPh₃)(CO)₃]₂²⁺**

Conformational energy plots
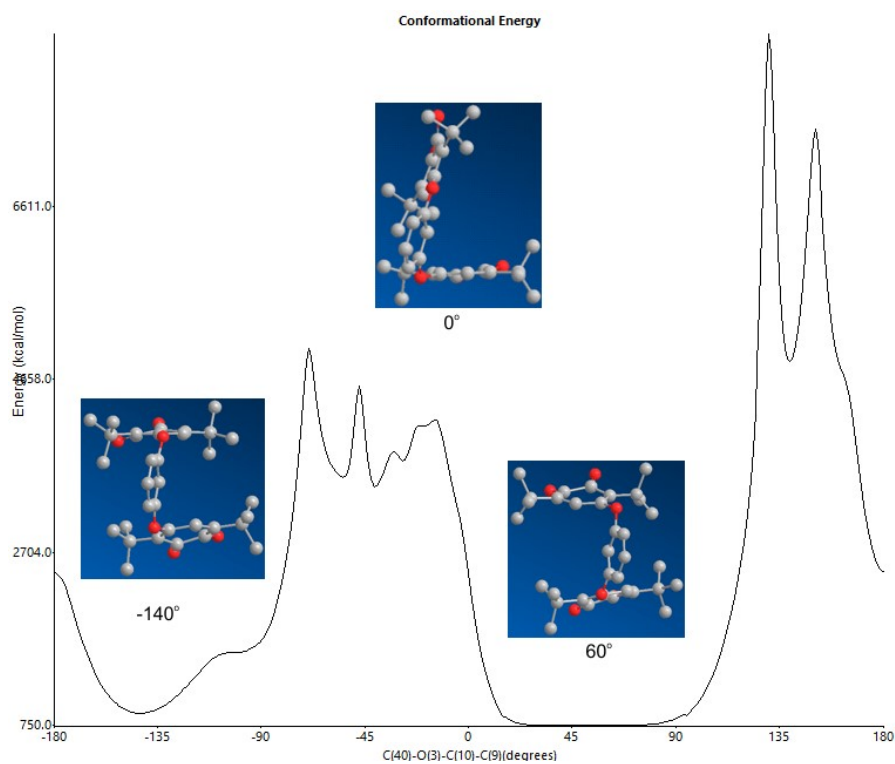
Figure SI20. Conformational energy plot performed by MM2+ technique for the rotation around **SQ-O** bond of **SQ-O-*Lnk*** hinge in **1**.
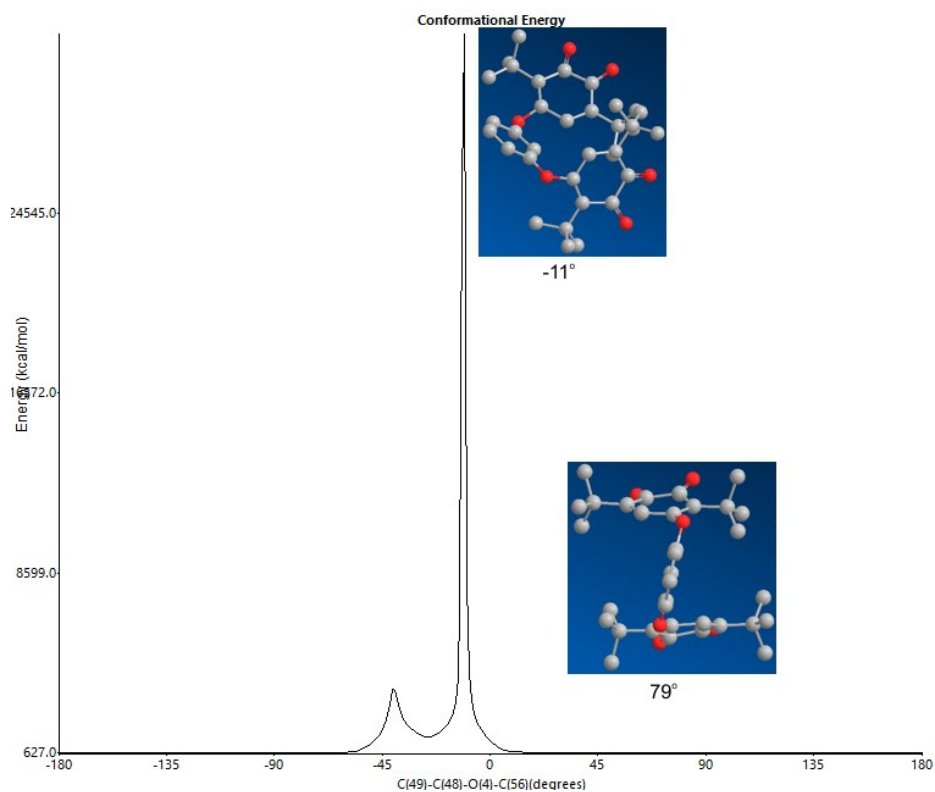
Figure SI21. Conformational energy plot performed by MM2+ technique for the rotation around **O-*Lnk*** bond of **SQ-O-*Lnk*** hinge in **1**.
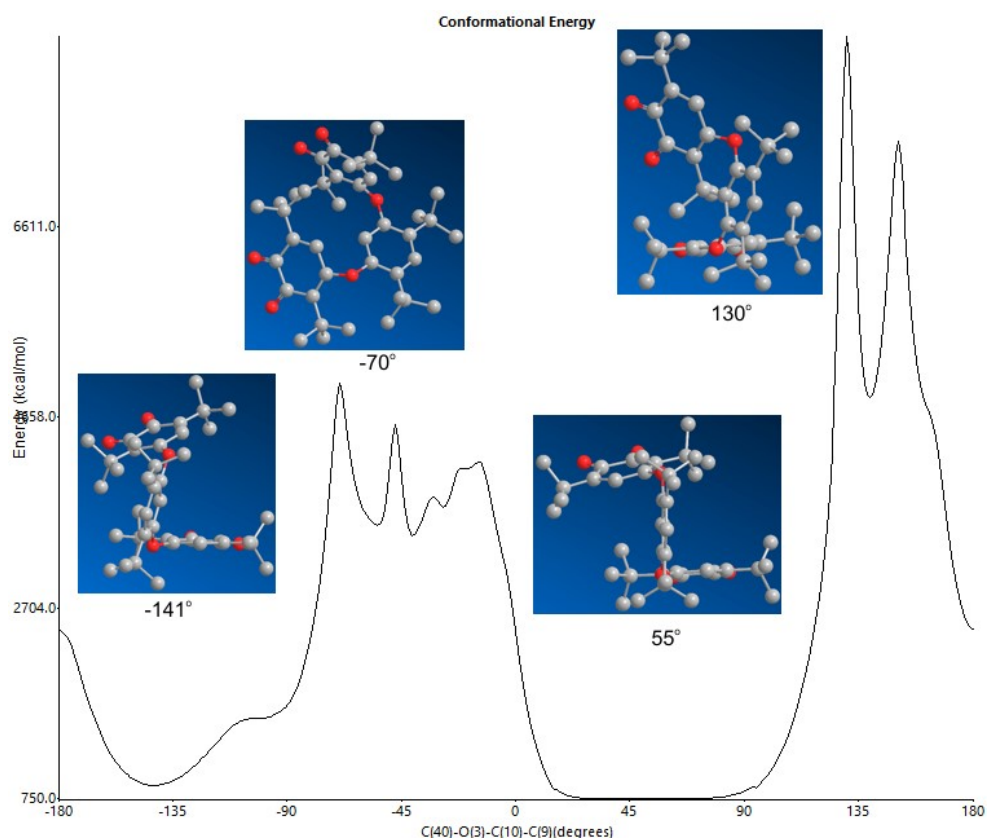
Figure SI22. Conformational energy plot performed by MM2+ technique for the rotation around **SQ-O** bond of **SQ-O-*Lnk*** hinge in **2**.
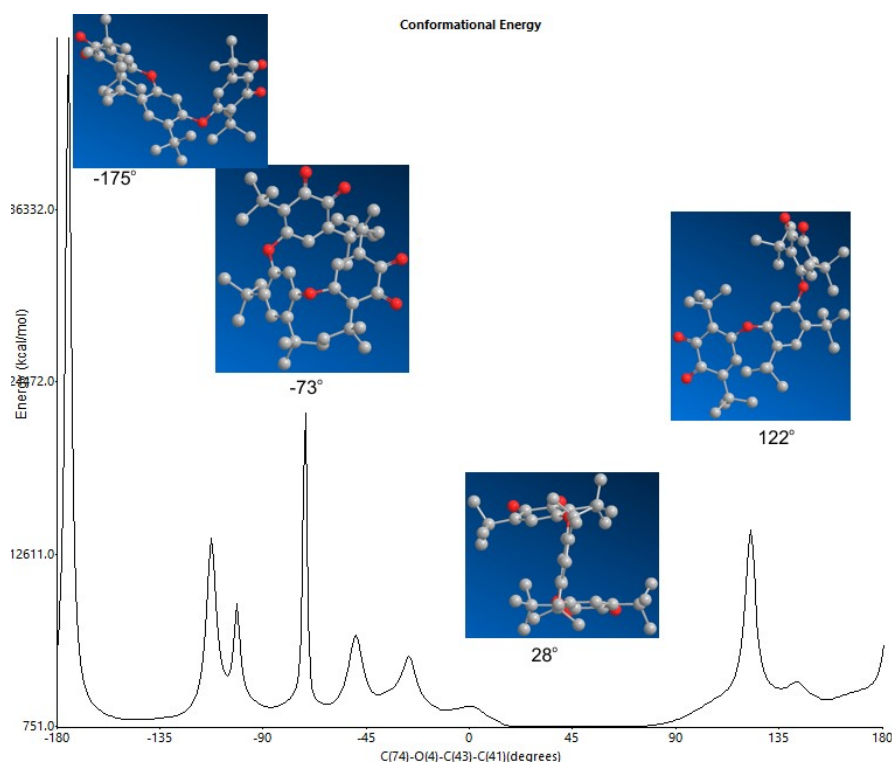
Figure SI23. Conformational energy plot performed by MM2+ technique for the rotation around **O-*Lnk*** bond of **SQ-O-*Lnk*** hinge in **2**.

NMR spectra
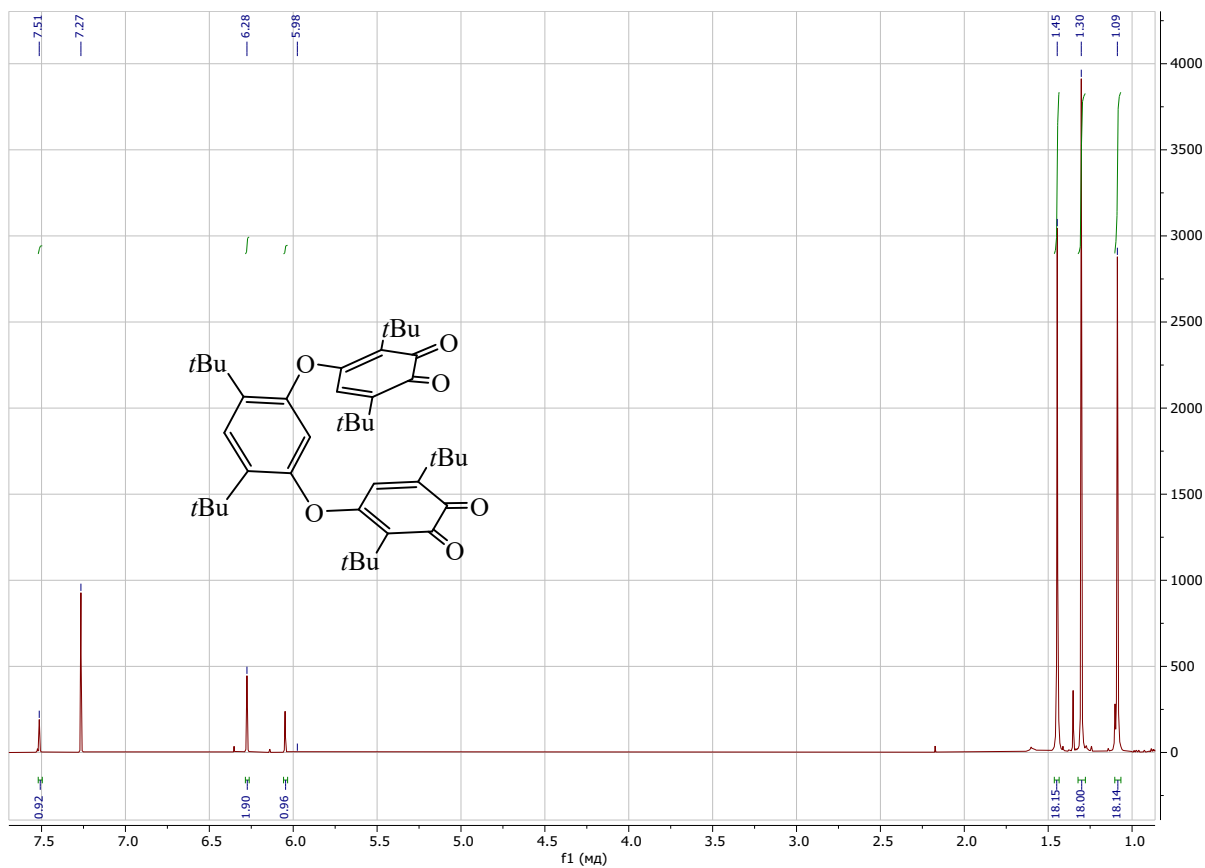
Figure SI24. ^{1}H NMR spectrum of **2** (CDCl$_3$)
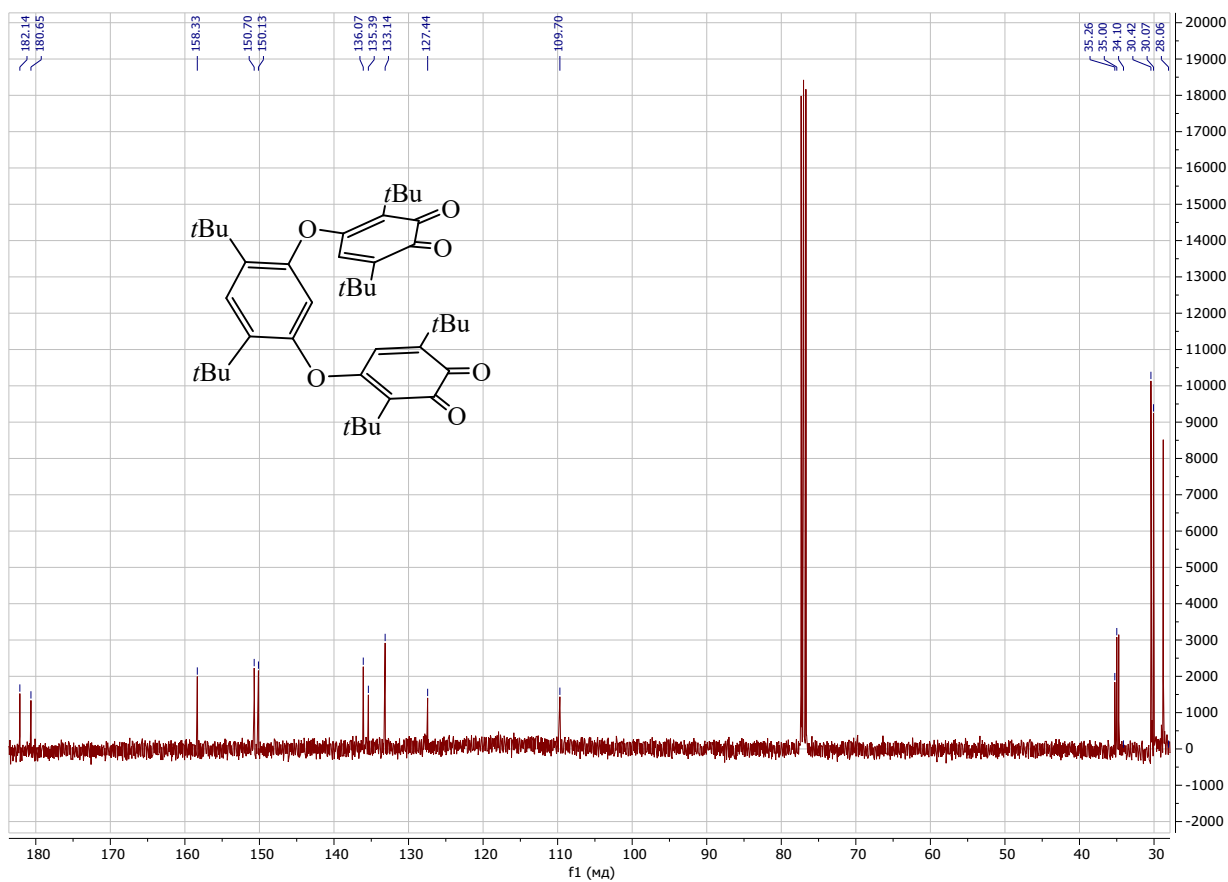
Figure SI25. ^{13}C NMR spectrum of **2** (CDCl$_3$)
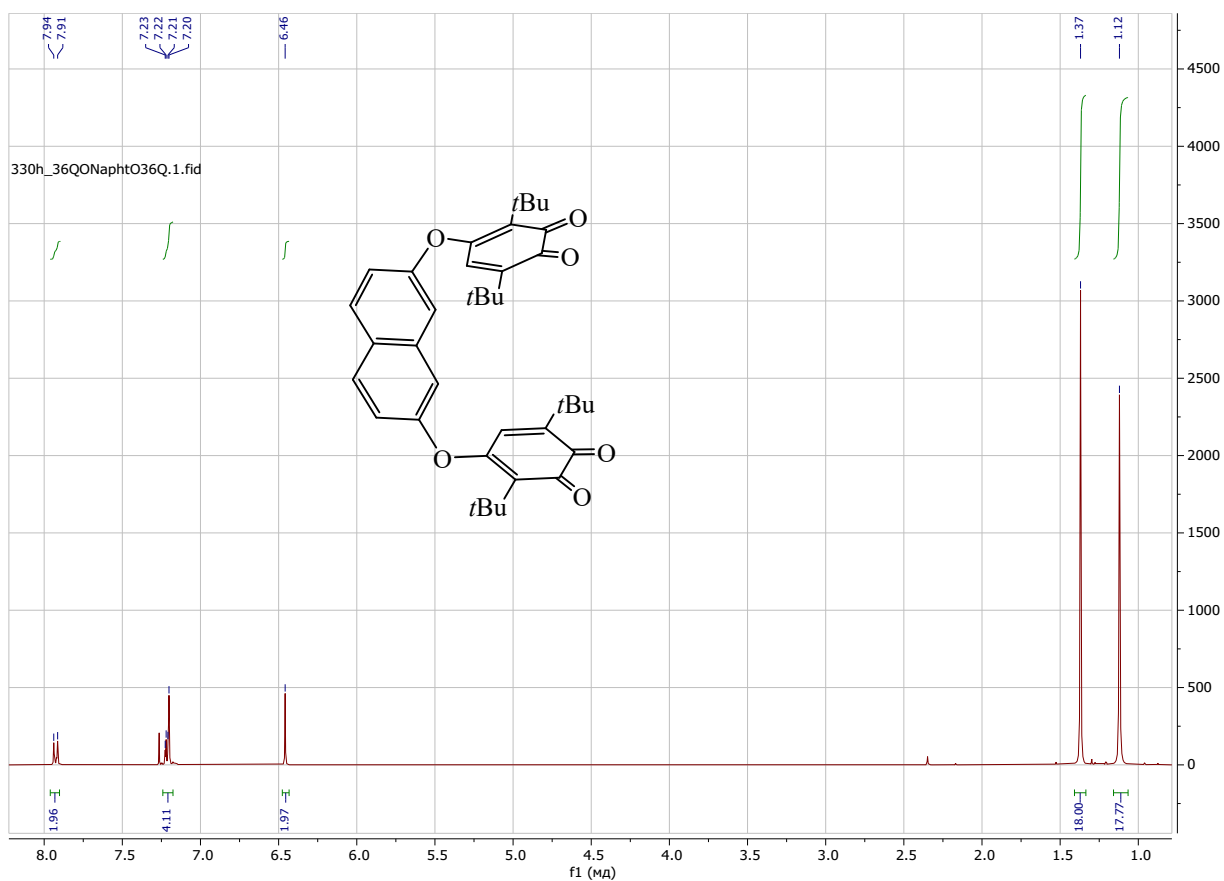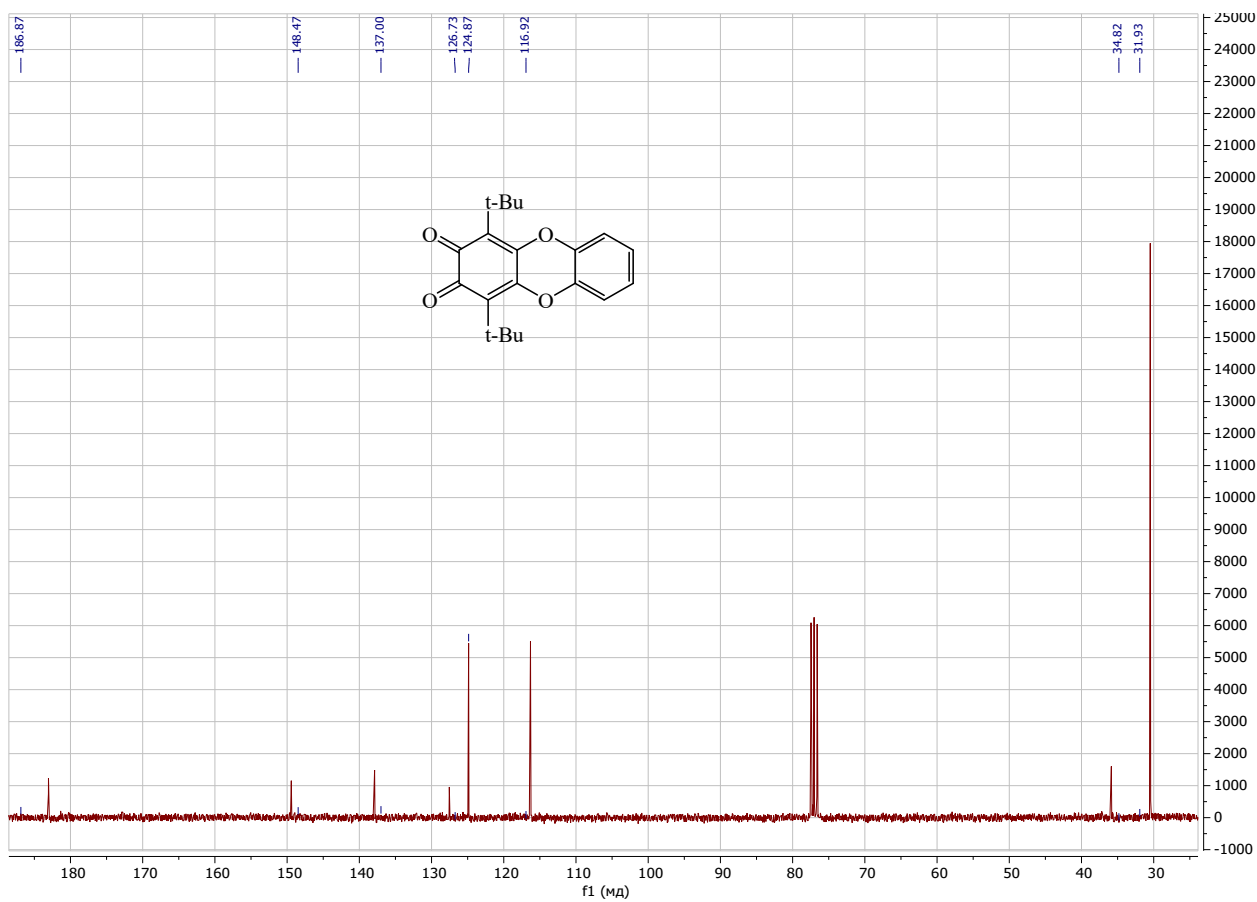
Figure SI26. ^{1}H NMR spectrum of **3** (CDCl$_3$)
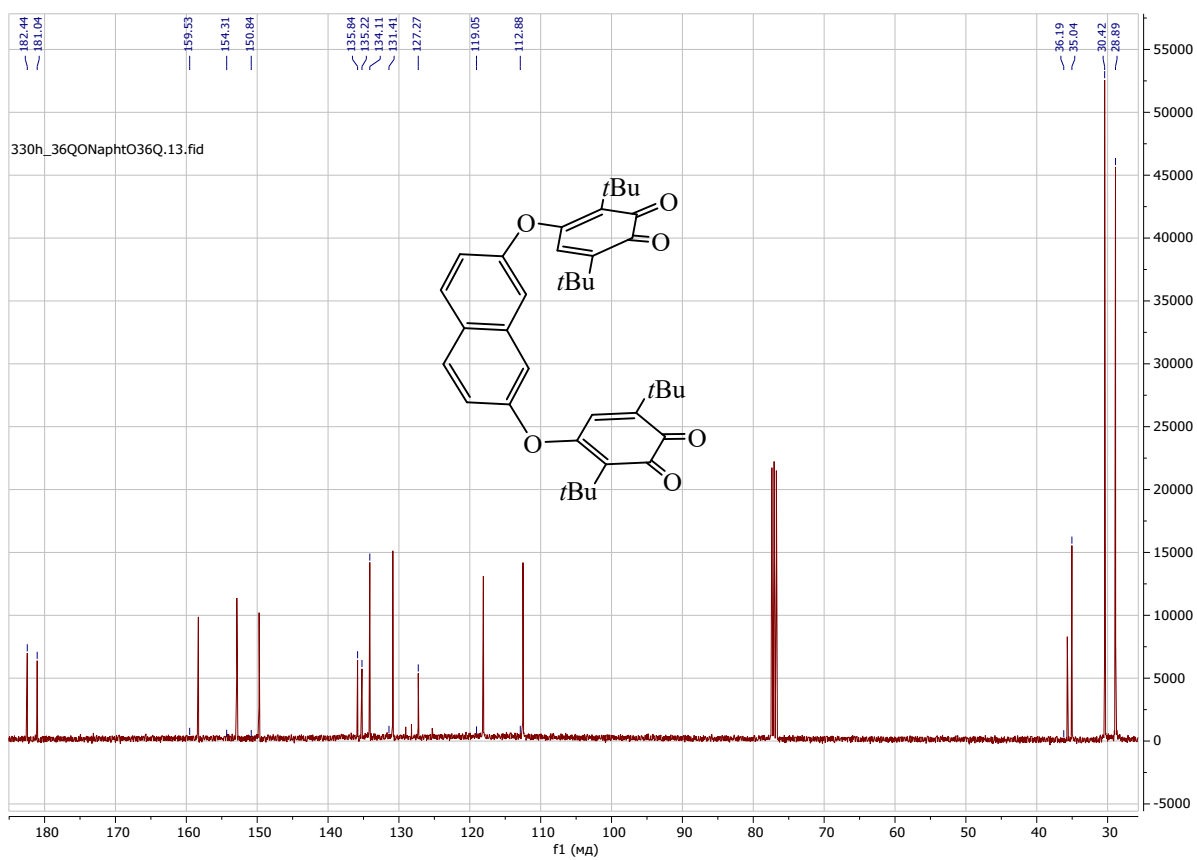
Figure SI27. ^{13}C NMR spectrum of **3** (CDCl$_3$)
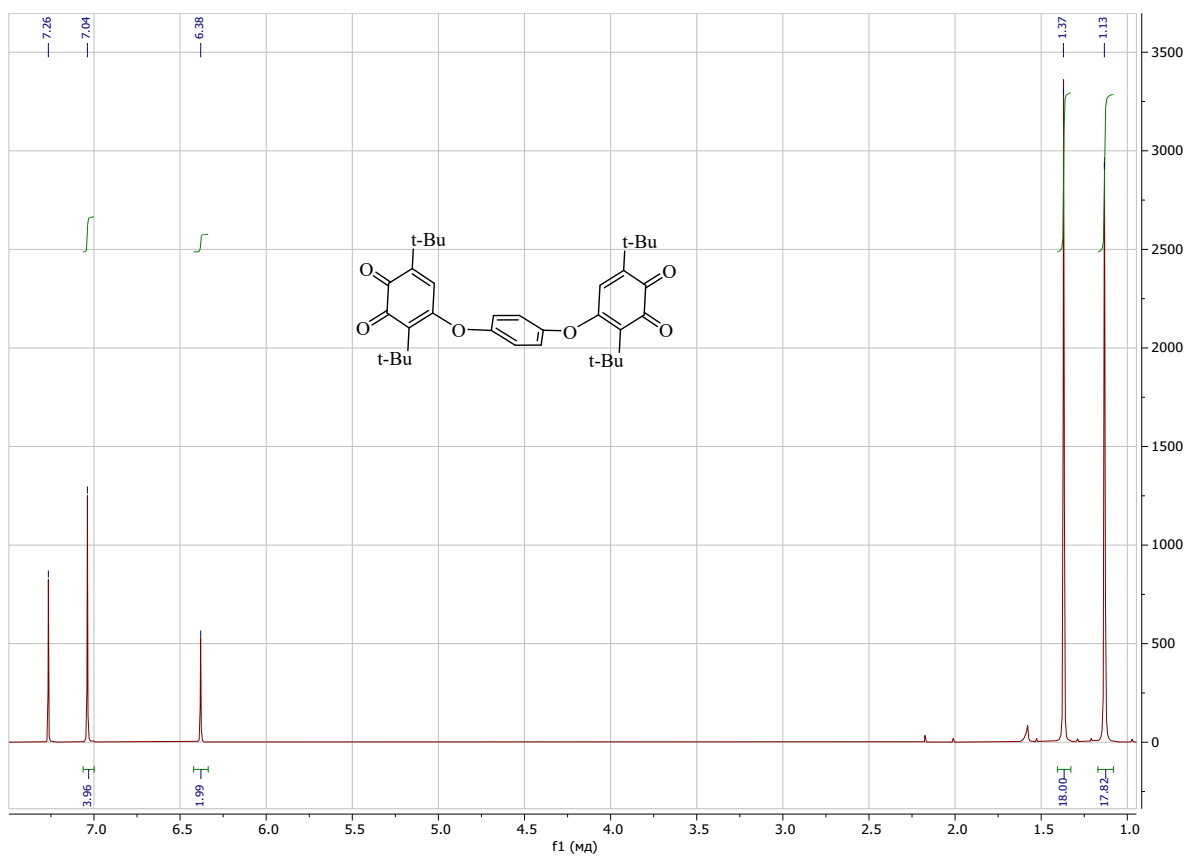
Figure SI28. ¹H NMR spectrum of **4** (CDCl₃)
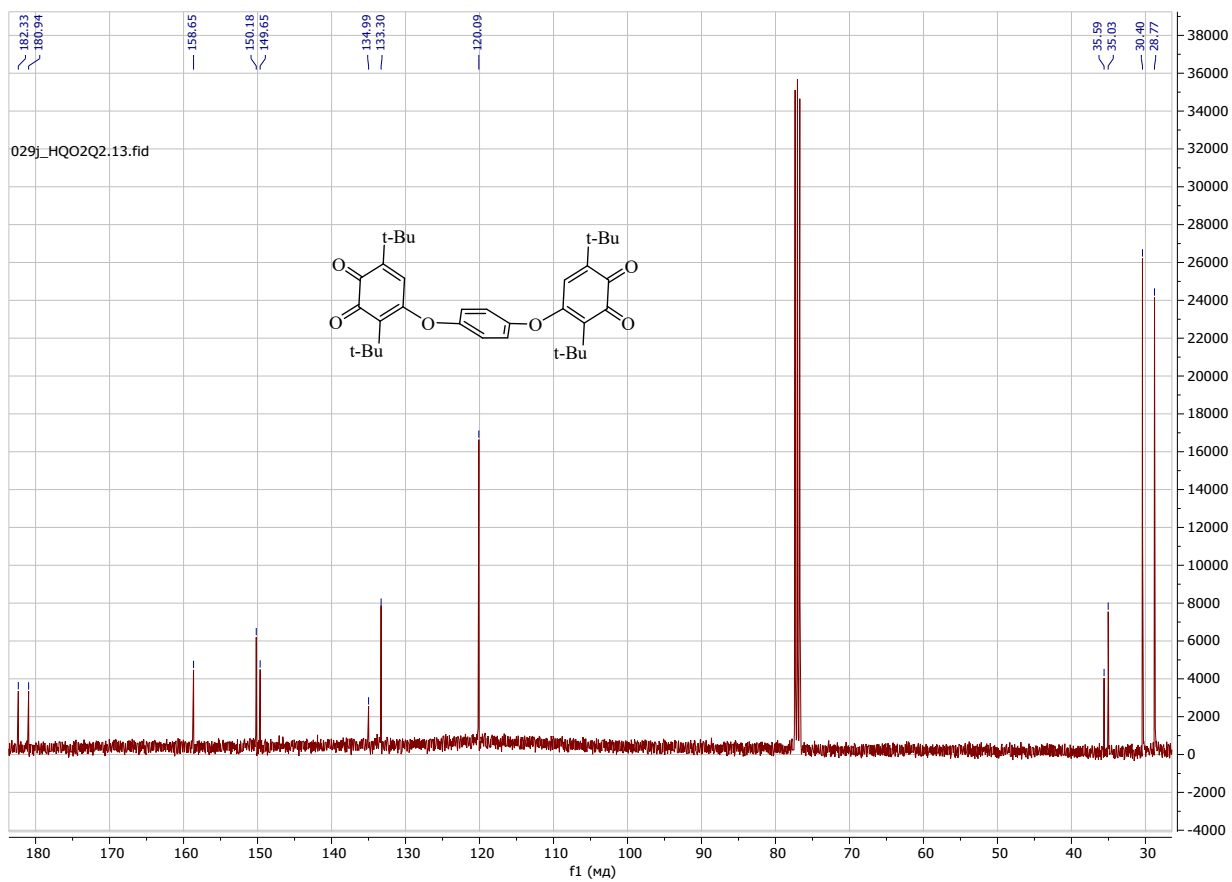
Figure SI29. ¹³C NMR spectrum of **4** (CDCl₃)
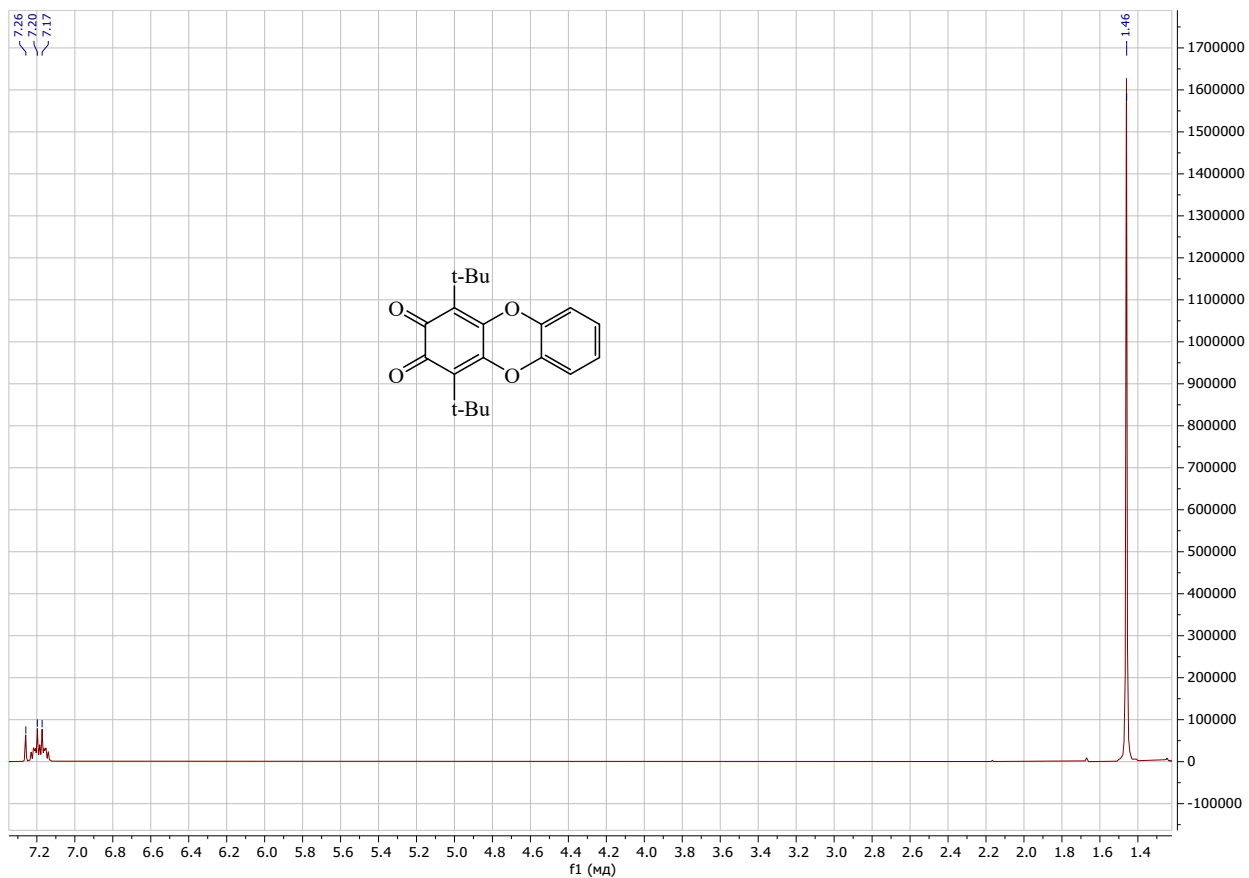
Figure SI30. ^{1}H NMR spectrum of **5** (CDCl$_3$)

Figure SI31. ^{13}C NMR spectrum of **5** (CDCl$_3$)

IR spectra
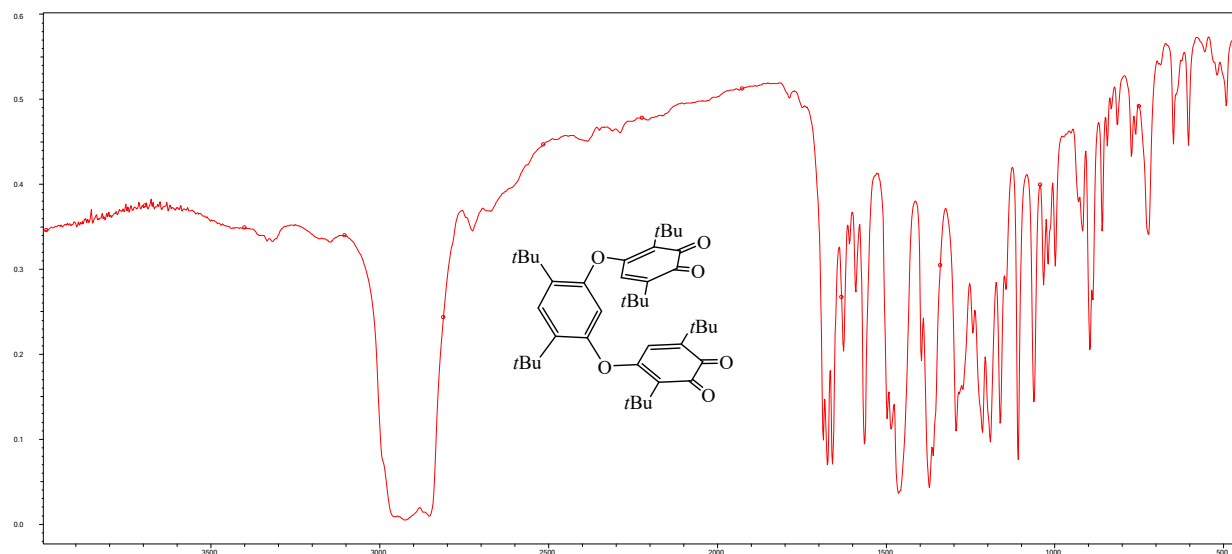
Figure SI32. IR spectrum of **2** (nujol)
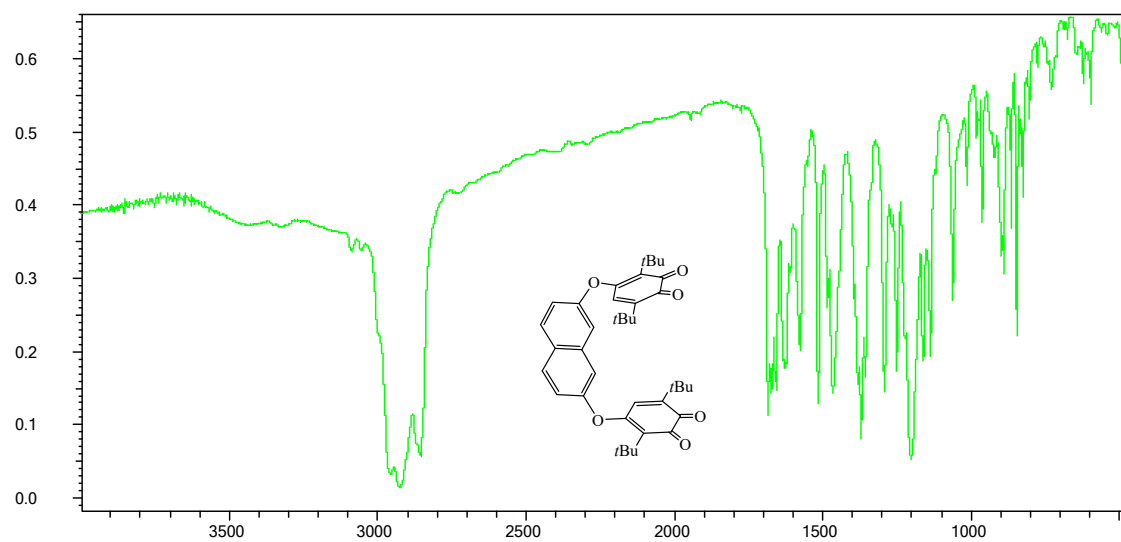
Figure SI33. IR spectrum of **3** (nujol)
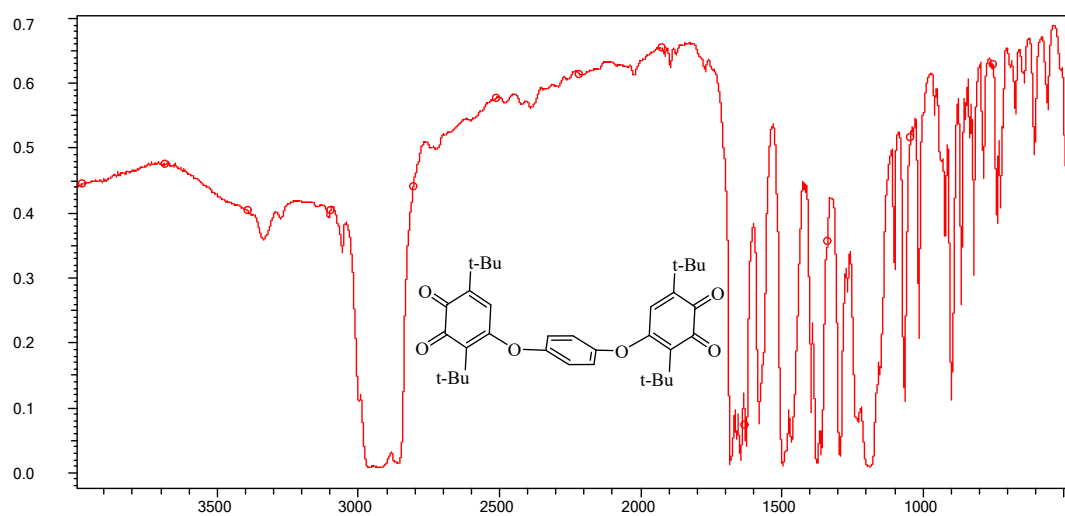
Figure SI34. IR spectrum of **4** (nujol)
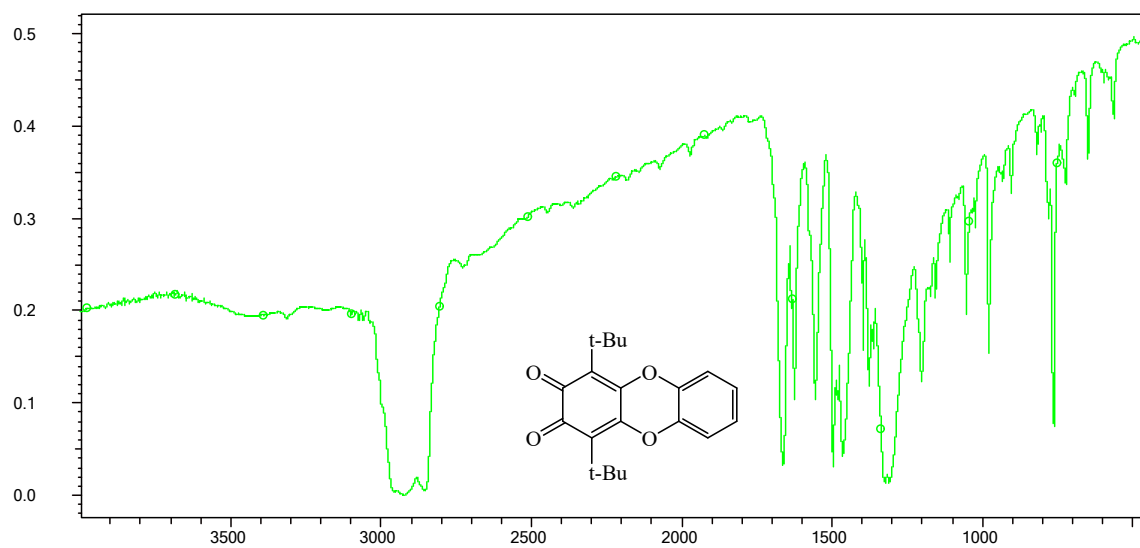
Figure SI35. IR spectrum of **5** (nujol)

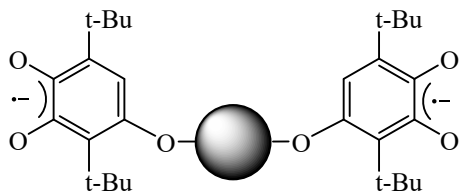**DFT calculations data for dianion biradical di-o-quinone species**

Table SI3. Relative electronic energies E_{el} (kcal/mol) of the triplet direduced quinone derivatives relative to triplet **1A²⁻** and energies of their frontier MOs (eV)

Dianion	E_{el}	$E_{(\alpha\text{-LUMO+1})}$	$E_{(\alpha\text{-LUMO})}$	$E_{(\alpha\text{-HOMO})}$	$E_{(\alpha\text{-HOMO-1})}$
1A²⁻	0	1.00	0.60	-3.13	-3.15
1²⁻	2.70	0.89	0.61	-3.01	-3.04
2²⁻	-	0.83	0.69	-2.96	-3.00
4²⁻	3.58	1.00	0.40	-3.04	-3.14

Table SI4 Relative electronic energies E_{el} (kcal/mol) of the open-shell singlet direduced quinone derivatives relative to triplet **1A²⁻** and energies of their frontier MOs (eV)

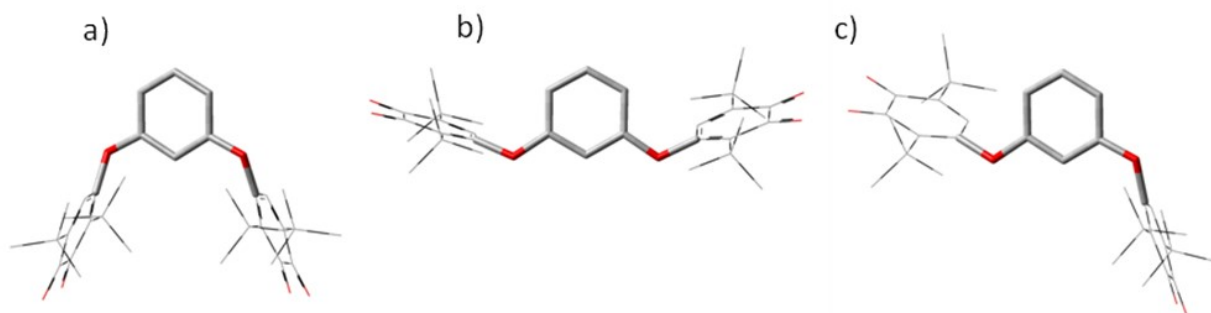| Direduced quinone derivative	Relative energies, kcal/mol	$E_{(\alpha\text{-HOMO})}$ eV	$E_{(\beta\text{-HOMO})}$ eV	$E_{(\alpha\text{-LUMO})}$ eV	$E_{(\beta\text{-LUMO})}$ eV
1A²⁻	0	-3.14	-3.14	-1.18	-1.18
1²⁻	2.70	-3.02	-3.02	-1.07	-1.08

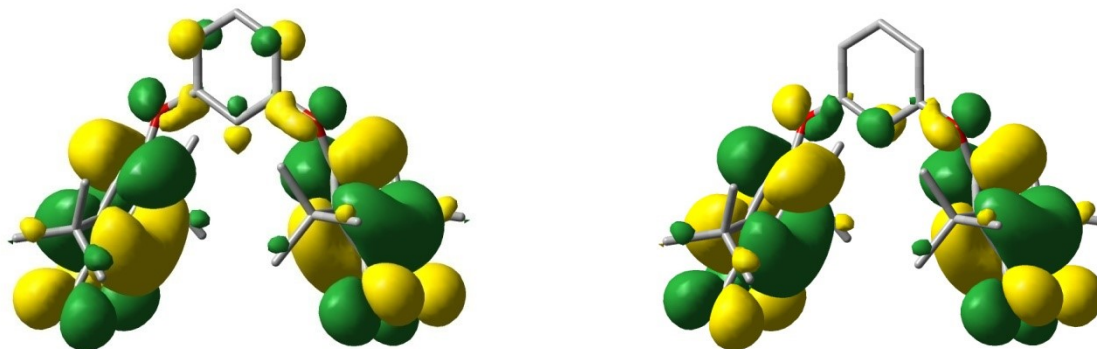Figure SI36. Optimized geometries of dianions: **1²⁻** (a), **1A²⁻** (b) and **1B²⁻** (c).

Figure SI37. Isosurfaces (isovalue 0.015) of the triplet **1²⁻** α-HOMO-1 (left) and α-HOMO (right).
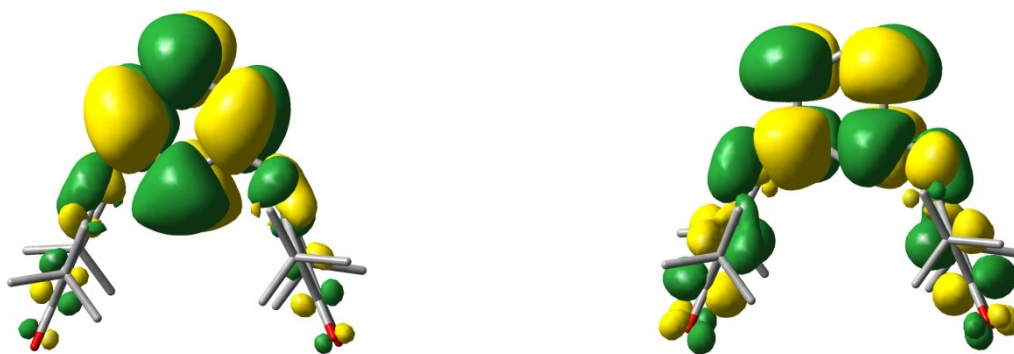
Figure SI38. Isosurfaces (isovalue 0.015) of the triplet $\mathbf{1}^{2-}$ α-LUMO (left) and α-LUMO+1 (right).
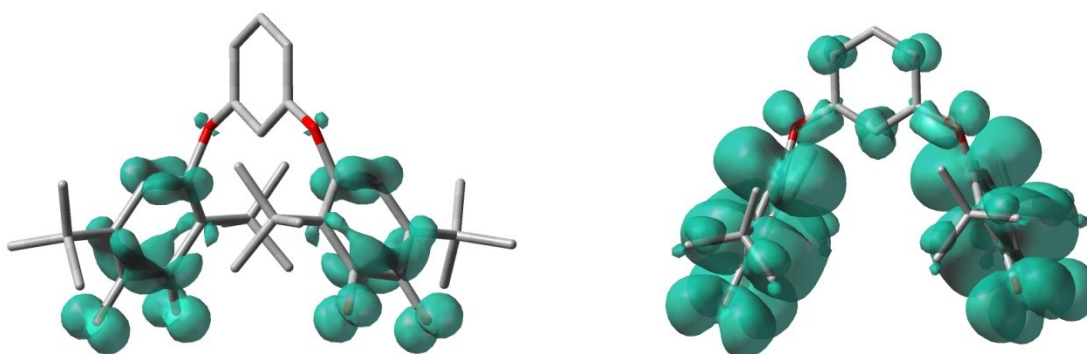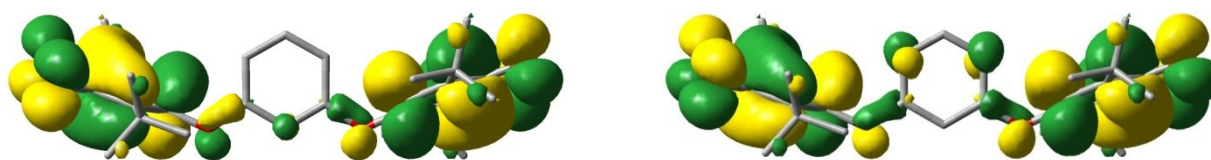

Figure SI39. Calculated α-spin density distribution in triplet $\mathbf{1}^{2-}$. Isovalue 0.005 a.u. (left) and 0.0002 a.u. (right).

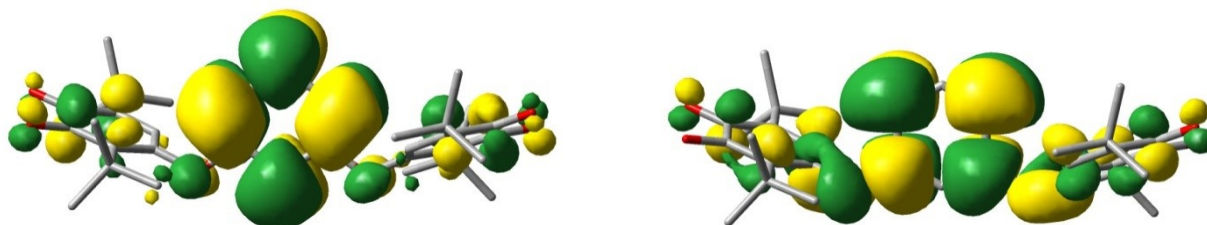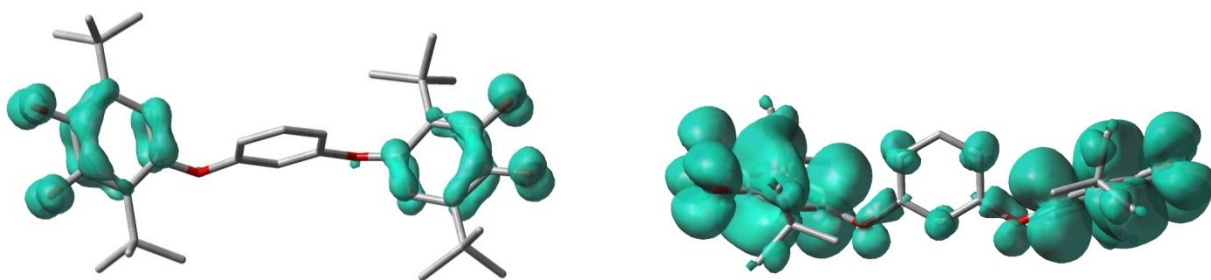Figure SI40. Isosurfaces (isovalue 0.015) of the triplet $\mathbf{1A}^{2-}$ α-HOMO-1 (left) and α-HOMO (right).

Figure SI41. Isosurfaces (isovalue 0.015) of the triplet $\mathbf{1A}^{2-}$ α-LUMO (left) and α-LUMO+1 (right).

Figure SI42. Calculated α-spin density distribution in triplet **1A²⁻.** Isovalue 0.005 a.u. (left) and 0.0002 a.u. (right).
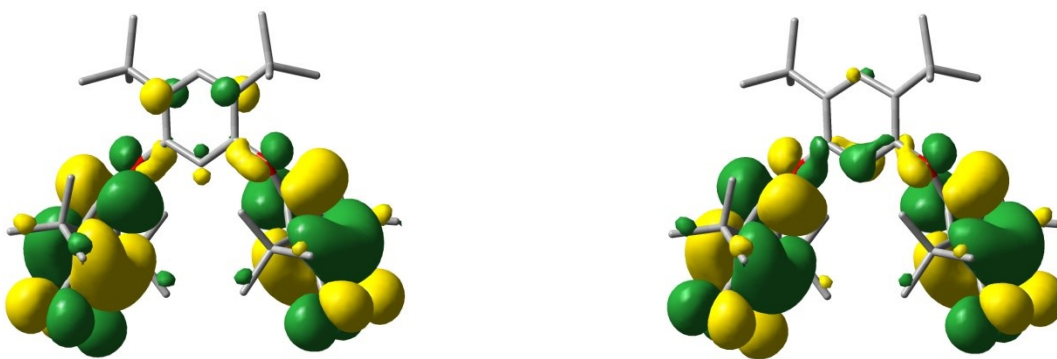

Figure SI43. Isosurfaces (isovalue 0.015) of the triplet **2²⁻** α-HOMO-1 (left) and α-HOMO (right).
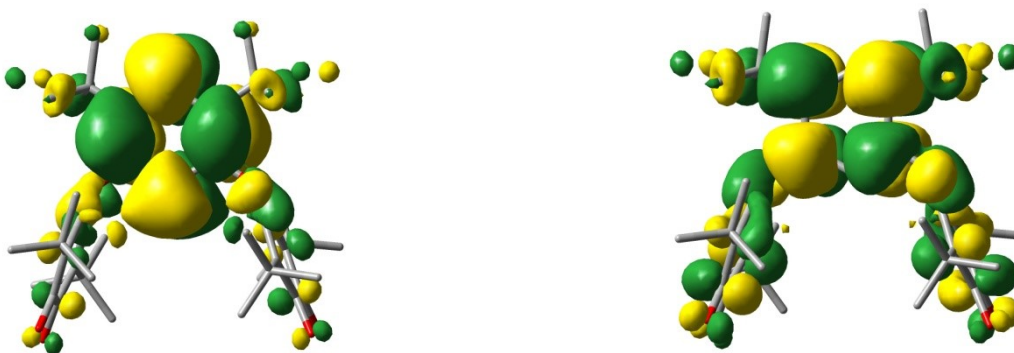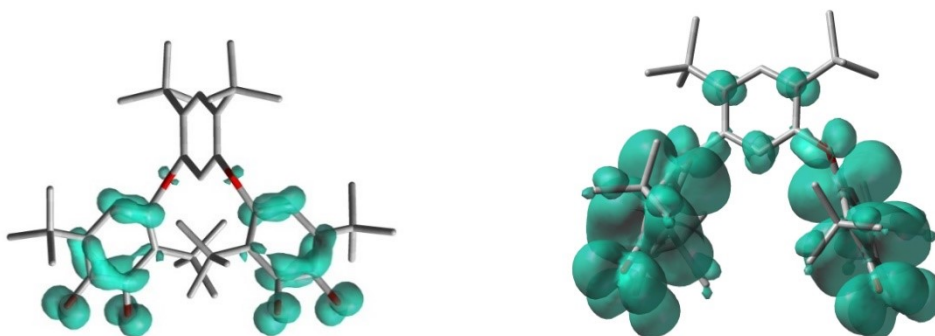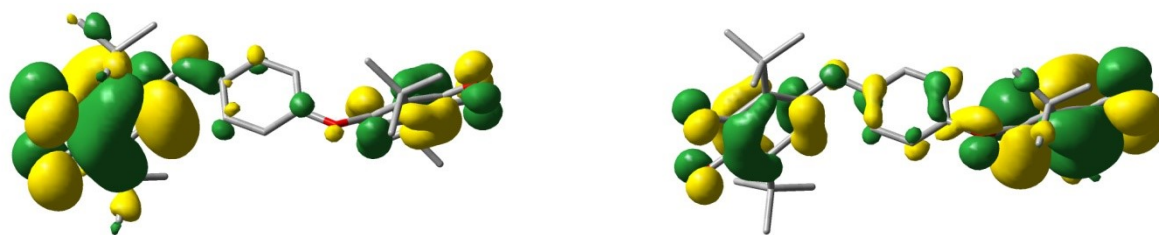

Figure SI44. Isosurfaces (isovalue 0.015) of the triplet **2²⁻** α-LUMO (left) and α-LUMO+1 (right).

Figure SI45. Calculated α-spin density distribution in triplet **2²⁻.** Isovalue 0.005 a.u. (left) and 0.0002 a.u. (right).

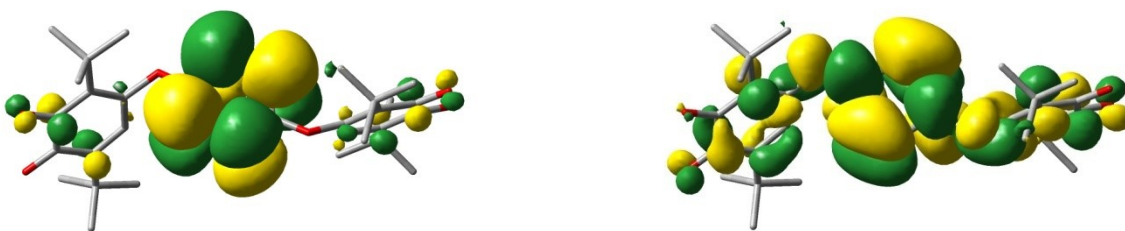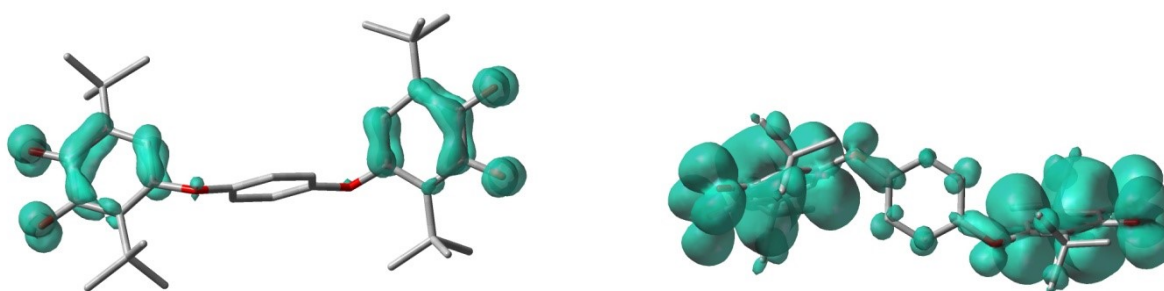Figure SI46. Isosurfaces (isovalue 0.015) of the triplet **4²⁻** α-HOMO-1 (left) and α-HOMO (right).

Figure SI47. Isosurfaces (isovalue 0.015) of the triplet **4²⁻** α-LUMO (left) and α-LUMO+1 (right).

Figure SI48. Calculated α-spin density distribution in triplet **4²⁻.** Isovalue 0.005 a.u. (left) and 0.0002 a.u. (right).
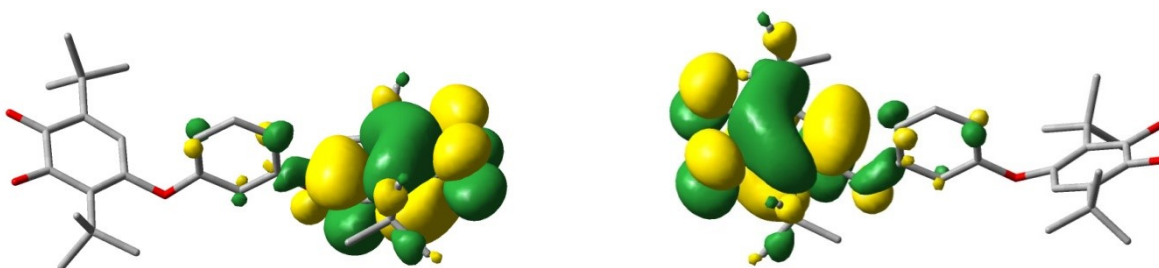

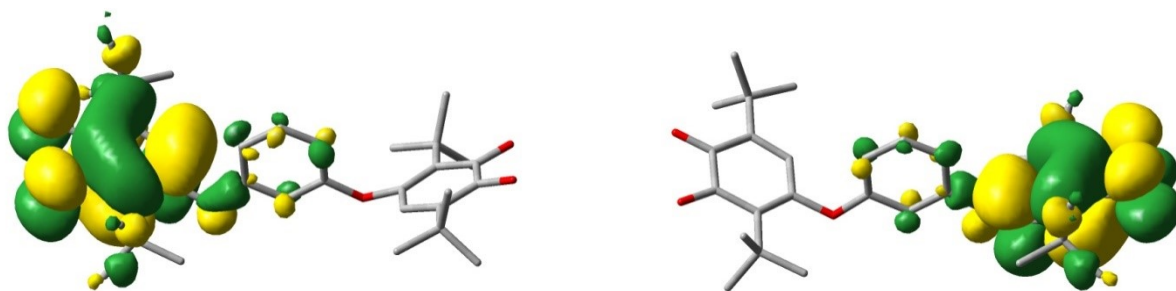Figure SI49. Isosurfaces (isovalue 0.015) of the open-shell singlet **1A²⁻** α-HOMO (left) and β-HOMO (right).

Figure SI50. Isosurfaces (isovalue 0.015) of the open-shell singlet $\mathbf{1A^{2-}}$ α-LUMO (left) and β -LUMO (right).
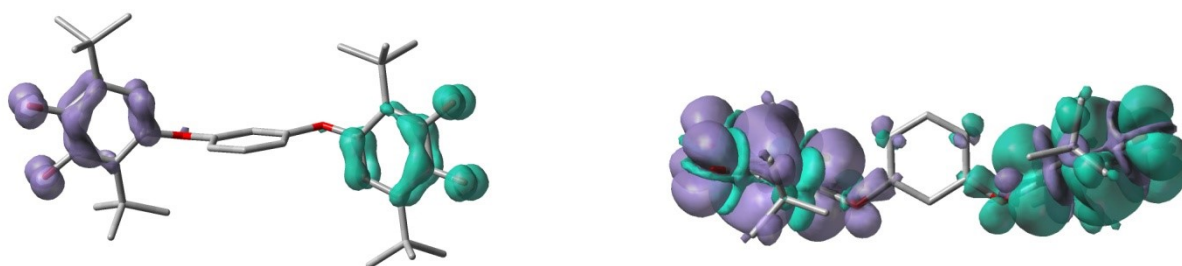

Figure SI51. Calculated α,β-spin density distribution in open-shell singlet $\mathbf{1A^{2-}}$. Isovalue 0.005 a.u. (left) and 0.0002 a.u. (right).
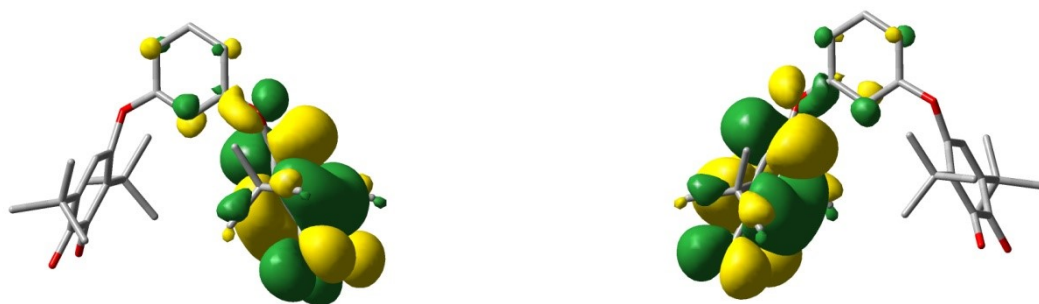

Figure SI52. Isosurfaces (isovalue 0.015) of the open-shell singlet $\mathbf{1^{2-}}$ α-HOMO (left) and β-HOMO (right).

Figure SI53. Isosurfaces (isovalue 0.015) of the open-shell singlet $\mathbf{1^{2-}}$ α-LUMO (left) and β -LUMO (right).
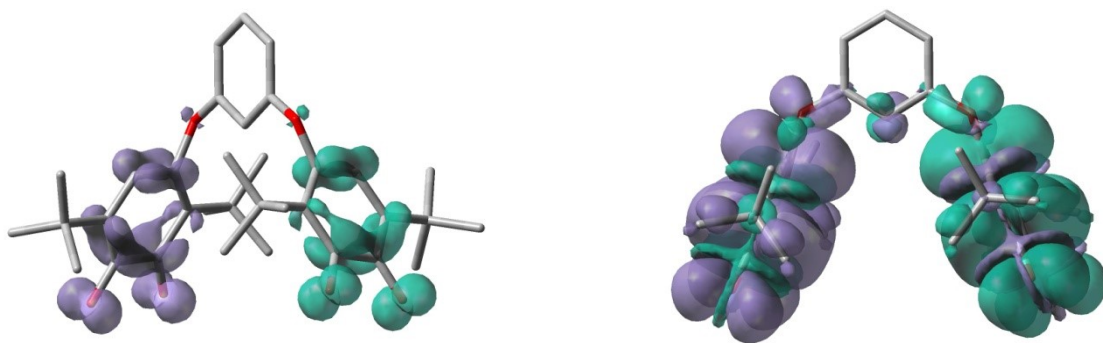
Figure SI54. Calculated α,β-spin density distribution in open-shell singlet **1²⁻.** Isovalue 0.005 a.u. (left) and 0.0002 a.u. (right).